Computers and Geotechnics 188 (2025) 107603

Contents lists available at ScienceDirect

Computers and Geotechnics

journal homepage: www.elsevier.com/locate/compgeo

Research Paper

A THM-coupled MPM framework for modelling rock-ice avalanches

Xiaoqin Lei [a,*], Siming He [a], Changbing Qin [b], Jidong Zhao [a,c,*], Gordon G.D. Zhou [a], Liu Ming [a]

[a] Key Laboratory of Mountain Hazards and Engineering Resilience, Institute of Mountain Hazards and Environment, CAS, Chengdu 610041, China
[b] School of Civil Engineering, Chongqing University, Chongqing 400044, China
[c] Dept of Civil and Environmental Engineering, HKUST, Hong Kong Special Administrative Region of China

ARTICLE INFO

Keywords:
Material point method
Rock-ice avalanches
Thermo-hydro-mechanical
Frictional heating
Thermal pressurization

ABSTRACT

Rock-ice avalanches exhibit hypermobility due to thermo-hydro-mechanical (THM) processes involving ice-water phase transitions, frictional heating, and thermal pressurization. They are typically characterized by high velocities and extended runout distance, posing significant hazards to human life and infrastructure in cold mountainous regions. This study presents a novel three-phase material point method (MPM) framework unifying THM coupling among skeleton deformation, pore water seepage, heat transfer, and ice-water phase change within the sliding rock-ice mixture. It also features a multi-material frictional contact model to describe the interactions of multiphase porous mixture with the basal terrain, accounting for frictional heating and thermal pressurization at the interface. The framework further introduces a shear band scaling technique to resolve sub-grid thermal-hydraulic processes. It is validated against (i) the classical freezing process in a semi-infinite porous medium, (ii) frictional heating in elastic/elastoplastic sliding blocks, and (iii) the 2016 Lamplugh rock-ice avalanche. The predictions demonstrate that thermal pressurization substantially reduces basal friction, reasonably explaining the extreme runout (10.5 km) at Lamplugh. The framework offers a unified prediction tool for simulating THM-driven hypermobility in complex terrains.

1. Introduction

As global warming accelerates and high-altitude engineering activities increase, glacial geological hazards, particularly rock-ice avalanches, are occurring frequently in high-altitude alpine regions (Richardson and Reynolds, 2000; Zhang et al., 2024). Among them, rock-ice avalanches, a type of high-speed, long-runout landslide containing ice debris, are characterized by their large volume, high velocity, and long travel distance, and have repeatedly caused catastrophic incidents that shock the world (Shugar et al., 2021; Zhao et al., 2021). In recent decades, the frequency and scale of rock-ice avalanches have been increasing worldwide, which pose significant threats to human lives and properties in those cold mountainous regions (Fan et al., 2021; Kääb et al., 2021).

Rock-ice avalanches are defined as rock and debris avalanches that involve ice or snow from initiation by the failure of high-mountain steep glaciers or the entrainment of ice along their propagation paths (Yang et al., 2019). Due to the presence of ice, rock-ice avalanches exhibit higher mobility compared to classic rock avalanches, which are characterized by lower friction of ice or snow surfaces and the lubrication or fluidization facilitated by meltwater (Pudasaini and Krautblatter, 2014). In the literature, lots of experimental studies have been conducted to understand how ice fragments affect the mobility of rock-ice avalanches. Schneider et al. (2011) and Dong et al. (2024) simulated the flow transition from solid to fluid state in rock-ice avalanches using rotating drum experiments, through which the evolution of friction coefficients during the flow of rock-ice granular mixtures, as well as the mechanism by which ice-water phase transitions affect flow regimes have been investigated. Yang et al. (2019) and Ren et al. (2021) conducted flume tests to examine how factors such as initial ice content, initial volume, mixing methods of rock-ice fragments, and meltwater films influence the runout and deposition behavior of rock-ice avalanches. Additionally, Fan et al. (2025) highlighted a possible rock-ice segregation mechanism contributing to the hypermobility of the avalanche, based on flume test results. These experiments can partially replicate the flow behavior of rock-ice avalanches and shed light on some mechanisms and factors

* Corresponding authors at: Key Laboratory of Mountain Hazards and Engineering Resilience, Institute of Mountain Hazards and Environment, CAS, Chengdu 610041, China.
E-mail addresses: xiaoqin.lei@imde.ac.cn (X. Lei), jzhao@ust.hk (J. Zhao).

https://doi.org/10.1016/j.compgeo.2025.107603
Received 1 August 2025; Received in revised form 19 August 2025; Accepted 25 August 2025
Available online 2 September 2025

contributing to the exceptional mobility of rock-ice avalanches. However, quantifying key processes, such as frictional heat-induced ice melting, remains challenging under current experimental conditions due to their strong dependence on scale effects.

Extensive numerical simulations have also been carried out to reproduce the flow dynamics of rock-ice avalanches. Most simulations simplify rock-ice avalanches as single-phase fluids and describe the runout characteristics by the classic depth-averaged shallow water equations with improved frictional models. Among these, Sosio et al. (2012) incorporated thermodynamic equations to estimate the basal frictional melting rates of ice fragments during sliding, while De Blasio (2014) further accounted for the influence of sliding body thickness on frictional melting and dynamic characteristics. To better reconstruct the solid-liquid phase transition and fluidization processes, Pudasaini and Krautblatter (2014) developed the first two-phase flow model that explicitly considers mass/momentum exchange between solid and liquid phases. Gnyawali et al., (2020) and Wang et al. (2023) subsequently applied this model to analyze solid-liquid evolution in actual rock-ice avalanche events. Based on Pudasaini and Krautblatter (2014)'s model, Sansone et al. (2021) further established a three-phase flow framework to explicitly distinguish solid ice and rock components, and Liu and He (2024) further incorporated an energy conservation equation to describe the evolution of mass temperature. Focusing on the thermo-hydro-mechanical (THM) coupling process within the shear band, He et al. (2021) and Wei et al. (2024) investigated THM-coupled effects in two rock-ice avalanche cases by integrating the sliding block model with THM-coupled formulations.

Rock-ice avalanches are essentially high-speed, long-runout landslides driven by THM-coupled processes during the extensive deformation of rock-ice granular mixtures. From this perspective, the above-mentioned depth-averaged approaches often oversimplify the intrinsic THM-coupled processes, while those sliding block models fail to capture the complex deformation behavior of the sliding mass. In recent years, meshless methods like the Material Point Method (MPM) (Bardenhagen et al., 2000) and Smoothed Particle Hydrodynamics (SPH) (Bui et al., 2008) have been widely adopted for landslide simulations. Among these methods, MPM has been demonstrated to be highly effective for simulating large deformations with multiphasic coupling effects (Soga et al., 2016). For example, Pinyol et al. (2018) have developed a THM-coupled MPM model for saturated soils to investigate thermal effects in landslide mobility. While Lei et al. (2021a, 2024) and Yu et al. (2024) developed THM-MPM models for unsaturated unfrozen soils and saturated frozen soils, none address the three-phase (rock/ice/water) coupling and basal thermal pressurization critical for rock-ice avalanches. This work bridges this gap by (i) proposing a three-phase THM-MPM formulation with ice-water phase change, (ii) integrating a multi-material contact algorithm for frictional heating and thermal pressurization, and (iii) introducing a shear band scaling method to model sub-grid processes.

Specifically, a novel MPM framework for modelling THM-coupled processes within rock-ice avalanches is proposed. Within this framework, a THM-coupled formulation is developed to capture the intricate processes of skeleton deformation, pore water seepage flow, heat transfer, and ice-water phase change within the sliding rock-ice mixture. Simultaneously, the sliding interactions between this multiphase porous continuum and the basal terrain are captured by a multi-material contact model that accounts for frictional heating and thermal pressurization effects. The framework is first validated by modelling the freezing process of a semi-infinite porous medium. Its thermal pressurization features are then illustrated by simulating the frictional heating process in two scenarios: an elastic rock-ice block sliding with controlled velocity, and an elastoplastic rock-ice mixture sliding on an inclined surface. Finally, the framework's capability in addressing engineering problems is showcased by successfully reproducing the dynamic runout process of the Lamplugh rock-ice avalanche and its intrinsic THM-coupled hypermobility mechanism.

2. THM-coupled MPM framework

2.1. Physical phenomena and conception

The core factor behind the hypermobility of rock-ice avalanches lies in the fact that their sliding mass is a granular mixture composed of randomly mixed ice fragments (including ice, snow, etc.), rock blocks, and soil particles formed during the avalanches. The ice fragments in the sliding mass are not only prone to the gradual disintegration and fragmentation commonly observed in non-icy granular flows, but also highly susceptible to rapid melting under extensive basal frictional heating (Schneider et al., 2011; Sosio et al., 2012). The presence of ice not only directly reduces its internal and basal friction coefficients but also transforms the mass flow into a series of complex THM-coupled processes. As illustrated by Fig. 1a, the granular skeleton, composed of ice and rock debris blocks, undergoes continuous shear deformation during avalanching along the basal terrain. This process, accompanied by frictional heating and ice-water phase transitions around the basal shear band, leads to an increasing liquid water content within the sliding mass. This meltwater further percolates through the granular skeleton's pore spaces, changing its mechanical properties and stress state, and enhancing heat transfer. It not only directly changes the effective stress and temperature distribution within the sliding mass but also, through mechanisms like thermal expansion and shear contraction, generates significant excess pore water pressure, thereby facilitating the liquefaction and fluidization of the sliding mass. Throughout these processes, the fragmentation and frictional melting within the rock-ice granular mixture continuously alter the mixture's gradation and solid-liquid composition, accelerating the shear deformation of the sliding body. Concurrently, the high-speed sliding of the debris mass further intensifies the internal fragmentation and frictional melting processes.

In this paper, a set of THM-coupled formulation is developed to capture these coupled processes occurring within the sliding rock-ice mixture. Simultaneously, a thermo-mechanical contact model is adopted to capture the sliding interactions between the rock-ice mixture and the basal sliding interface. These two components are implemented with a unified THM-coupled MPM framework, which can interact with each other to capture the complex THM-coupled behaviour during rock-ice avalanches.

As shown in Fig. 1b, the sliding mass of the rock-ice avalanche is mathematically treated as a three-phase porous medium, consisting of solid rock grains (S), liquid water (L), and ice crystals (I) phases. Within the framework of continuum mixture theory (Coussy, 2004), the representative elementary volume (REV), being heterogeneous at the microscopic scale with their intrinsic densities ρ_α, can be viewed as the superimposition of three phase particles which simultaneously occupy the whole REV volume with their corresponding apparent densities ρ^α (Lei et al., 2014). The apparent densities ρ^α are linked to their corresponding intrinsic densities ρ_α through their respective volume fractions n_α via $\rho^\alpha = n_\alpha \rho_\alpha$. The corresponding volume fractions of each phase can be defined as:

$$n_S = 1 - n; \quad n_I = n(1 - S_L); \quad n_L = nS_L \tag{1}$$

where n is the porosity of the rock-ice mixture; S_L is the liquid saturation. Further, the effective solid volume fraction n_S^e is introduced to represent the rock and ice volume fraction distribution together based on rock density (Pudasaini and Krautblatter, 2014):

$$n_S^e = \frac{(n_S \rho_S + n_I \rho_I)}{\rho_S} \tag{2}$$

As the density of the ice is much lower than the density of the rock, their density ratio in the above equation can be assumed as $\rho_S/\rho_I \approx 3$ for simplicity.

During the THM-coupled processes, all phase temperatures within the REV are equal by assuming local thermodynamic equilibrium. The

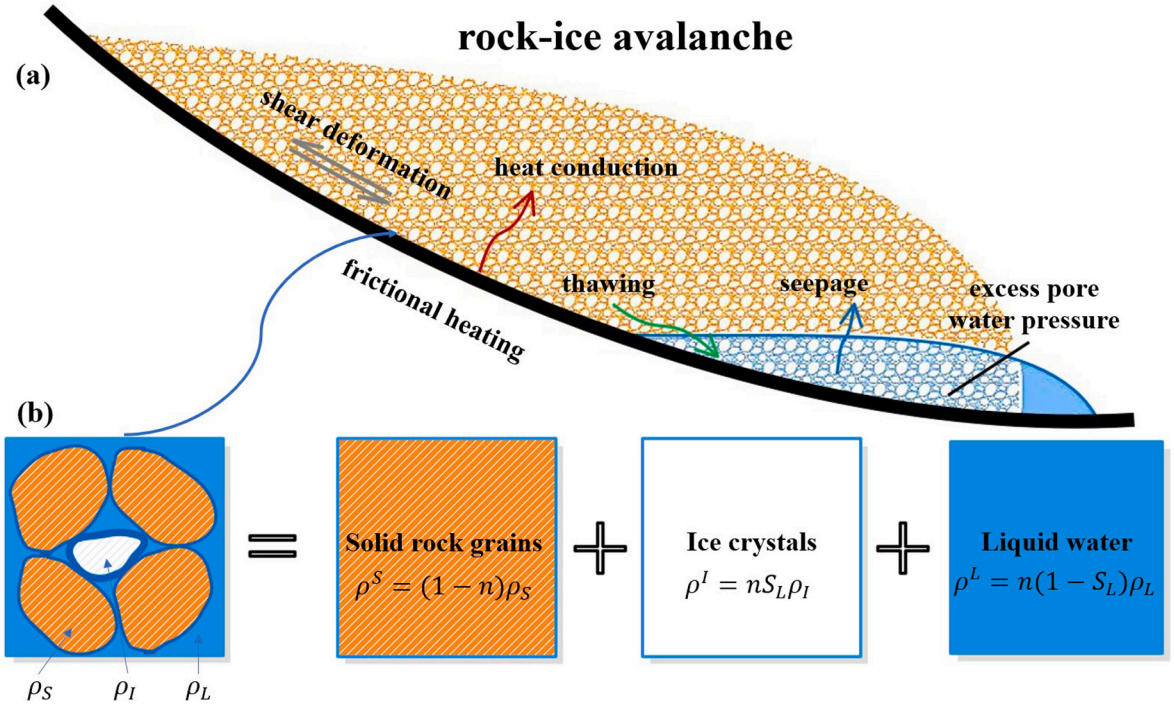

Fig. 1. (a) Key physical mechanisms underlying rock-ice avalanche and (b) the conception of rock-ice mixture as a tri-phasic granular medium.

intrinsic density of each phase are assumed can be linked with the temperature T and pore liquid pressure P_L via the following state equations (Yu et al., 2024):

$$\frac{d\rho_S}{\rho_S} = -\beta_S dT; \quad \frac{d\rho_I}{\rho_I} = -\beta_I dT; \quad \frac{d\rho_L}{\rho_L} = \frac{dP_L}{K_L} - \beta_L dT \tag{3}$$

where β_α are the volumetric thermal expansion coefficient for each phase. K_L is the bulk modulus of the liquid phase, which accounts for the compressibility of liquid under the pore liquid pressure P_L. Furthermore, when ice and liquid phases coexist in the pore, the Clapeyron equation is assumed to be valid, which links the pore liquid pressure P_L with the pore ice pressure P_I via (He et al., 2023):

$$P_L = \frac{\rho_L}{\rho_I}P_I - \rho_L L_f ln\frac{T+273.15}{T_{ref}+273.15} \tag{4}$$

where L_f is the latent heat of the formation of ice; T_{ref} is the freezing point of bulk water (thawing point of ice), which is generally set to 0°C.

2.2. THM-coupled model of the rock-ice mixture

2.2.1. Mass balance equations

At an arbitrary time t, the local form of the mass conservation for each phase within a given REV of the rock-ice mixture can be stated as (Coussy, 2004):

$$\frac{d^\alpha}{dt}(n_\alpha\rho_\alpha) + n_\alpha\rho_\alpha\nabla\cdot\boldsymbol{v_\alpha} = \dot{m}_\alpha \tag{5}$$

where $\frac{d^w}{dt}(*) = \frac{\partial}{\partial t}(*) + \nabla(*)\cdot\boldsymbol{v}_\alpha$ $(\alpha = S, I, L)$ is the particle derivative with respect to the phase α, with $\boldsymbol{v}_\alpha$ being the velocity associated with this specific phase. $\dot{m}_\alpha$ is the mass increase rate of each phase due to ice-water phase change. In this work, it is assumed that there is no mass exchange between the mixture and the surrounding environment, and only the phase change between ice and water is considered, hence $\dot{m}_S = 0$ and $\dot{m}_L = -\dot{m}_I$.

By assuming the solid density gradient within the REV is sufficient small ($\nabla\rho_S \approx 0$), the combination of the state equation for solid density Eq.(3) with the mass conservation equation for the solid phase leads to the following porosity evolution law (Lei et al., 2021a):

$$\frac{d^S n}{dt} = (1-n)\nabla\cdot\boldsymbol{v}_S - (1-n)\beta_S\frac{\partial T}{\partial t} \tag{6}$$

According to the equation, porosity change as a consequence of both mechanical deformation and thermal expansion. By assuming the ice phase is immobile relative to the solid skeleton ($\boldsymbol{v}_I \approx \boldsymbol{v}_S$), the addition of the mass conservation equations for both the ice and water phases in Eq. (5) could cancel their corresponding mass increase terms $\dot{m}_\alpha$, which leads to:

$$\begin{aligned}&[S_L\rho_L + (1-S_L)\rho_I]\frac{d^S n}{dt} + nS_L\frac{d^S\rho_L}{dt} + n(1-S_L)\frac{d^S\rho_I}{dt} + n(\rho_L-\rho_I)\frac{d^S S_L}{dt}\\ &+\nabla\cdot[nS_L\rho_L(\boldsymbol{v}_L-\boldsymbol{v}_S)] + [nS_L\rho_L + n(1-S_L)\rho_I]\nabla\cdot\boldsymbol{v}_S = 0\end{aligned} \tag{7}$$

By using the porosity evolution law Eq. (6), the state equation for ice and water densities Eq. (3), and neglecting the liquid density gradient $\nabla\rho_L \approx 0$, the above mass conservation equation for both liquid and ice phases can lead to the following pore liquid pressure equation:

$$\begin{aligned}\frac{d^S}{dt}P_L = \frac{K_L}{nS_L}\Bigg\{&\left[S_L + (1-S_L)\frac{\rho_I}{\rho_L}\right]\nabla\cdot\boldsymbol{v}_S + \Bigg[\beta_m - n\Bigg(1\\ &-\frac{\rho_I}{\rho_L}\Bigg)\frac{\partial S_L}{\partial T}\Bigg]\frac{\partial T}{\partial t} - \nabla\cdot\boldsymbol{q}_L\Bigg\}\end{aligned} \tag{8}$$

which relates the pore liquid pressure variation P_L to the skeleton deformation $\nabla\cdot\boldsymbol{v}_S$, the thermal change rate $\frac{\partial T}{\partial t}$, and the pore liquid seepage flux $\boldsymbol{q}_L$ (defined as $\boldsymbol{q}_L = nS_L(\boldsymbol{v}_L - \boldsymbol{v}_S)$). In the above, the term β_m is calculated with $\beta_m = (1-n)\left[S_L + (1-S_L)\frac{\rho_I}{\rho_L}\right]\beta_S + nS_L\beta_L + n(1-S_L)\frac{\rho_I}{\rho_L}\beta_I$, which summarises the contributions related to thermal expansion coefficients. The pore liquid seepage flux $\boldsymbol{q}_L$ is assumed to be driven solely by the pore liquid pressure gradient, *i.e.* $\boldsymbol{q}_L = -\frac{k_L}{\gamma_L}\nabla P_L$, with k_L being the hydraulic conductivity and γ_L being the specific weight of water. In this work, the shear band is idealized as a frictional contact behaviour between the sliding mass and the basal terrain. For

simplicity's sake, we will focus on the excess pore pressure due to frictional heating-induced thermal pressurization along the contact surface, and the excess pore liquid pressure contribution related to $\nabla\cdot\boldsymbol{v}_S$ in the sliding mass is assumed can be dropped in what follows.

2.2.2. Energy conservation equation

By assuming equal temperatures for the phases within the whole mixture, the energy conservation equation of the rock-ice mixture can be expressed as (Bekele et al., 2017; Yu et al., 2024):

$$\left[(\rho C_v)_m + \rho_I n L_f \frac{\partial S_L}{\partial T}\right]\frac{d^S T}{dt} + \rho_L C_L \boldsymbol{q}_L\cdot\nabla T + \nabla\cdot\boldsymbol{q}_T - q_s = 0 \tag{9}$$

where $(\rho C_v)_m = \sum_{\alpha=S,L,I} n_\alpha \rho_\alpha C_\alpha$ is the heat capacity per unit volume of the porous mixture. The second term in the bracket is the thermal contribution related to the latent heat of ice-water phase transition, with L_f being the latent heat of the formation of ice. $\frac{\partial S_L}{\partial T}$ is governed by the soil freezing characteristic curve (SFCC), which is assumed depend only on the temperature T in this work. The third term is the thermal contribution due to liquid advection $\boldsymbol{q}_L$. The fourth term is the thermal contribution due to pure diffusion $\boldsymbol{q}_T$, calculated by the Fourier's law $\boldsymbol{q}_T = -k_{Tm}\nabla T$, with $k_{Tm} = \sum_{\alpha=S,L,I} n_\alpha k_{T\alpha}$ being the thermal conductivity coefficient of the mixture. The fourth term q_s is the thermal contribution due to the heat source per unit volume, which is related to the frictional heating mechanism in this work (Lei et al., 2024).

2.2.3. Momentum balance equation

Following Pinyol et al. (2018) and Lei et al. (2024), the relative acceleration of liquid and ice with respect to the solid skeleton is assumed can be neglected for the sliding porous mixture. The momentum balance equation governing the kinematics of the sliding rock-ice mixture can be expressed as:

$$\rho\boldsymbol{a} = \nabla\cdot\boldsymbol{\sigma} + \rho\boldsymbol{b} \tag{10}$$

where $\boldsymbol{a}$ is the acceleration of the sliding rock-ice mixture; ρ is the mixture density, which can be represented as $\rho = \sum_{\alpha=S,L,I} n_\alpha \rho_\alpha$; $\boldsymbol{b}$ is the body force acceleration; $\boldsymbol{\sigma}$ is the total stress tensor, which can be calculated with the isotropic elastoplastic constitutive model with the following Mohr-Columb yield function F:

$$F = \frac{1}{2}(\boldsymbol{\sigma}_1 - \boldsymbol{\sigma}_3) - \frac{1}{2}(\boldsymbol{\sigma}_1 + \boldsymbol{\sigma}_3)sin\varphi + ccos\varphi \tag{11}$$

where $\boldsymbol{\sigma}_1$ and $\boldsymbol{\sigma}_3$ are the maximum and minimum principal effective stresses, respectively; φ and c are the internal friction angle and cohesion of the mixture, respectively.

2.3. MPM framework with thermal pressurization

Within the three-phase single-point MPM framework (Yerro et al., 2015; Lei et al., 2021a; Yu et al., 2024), the sliding rock-ice mixture, treated as a three-phase porous medium, is represented by a cloud of Lagrangian material points, while an Eulerian background grid is employed to solve the THM-coupled governing equations (Fig. 2). For simplicity, the basal terrain on which the mixture slides is treated as a static rigid material. The frictional contact between the sliding rock-ice mixture and this rigid base is simulated using the generalized multi-material contact algorithm with frictional heating (Nairn et al., 2018).

To model landslide hypermobility resulting from frictional heating, we primarily focus on the evolution of temperature and pore liquid pressure within the shear band adjacent to the sliding surface. Following Lei et al. (2024), the first layer of cells closest to the rigid base is deemed as the shear band layer. By using the classic linear MPM shape function for extrapolating temperature and pore pressure field variables for this layer, the variations of temperature and pore pressure on the contact nodes would only relate to the material points within the first layer of cells closest to them. Further, shear band thickness is typically in the millimetre or centimetre range, which is often smaller than the mesh resolution (scale of several meters) feasible for realistic landslide modelling. To approximate the temperature and pore pressure evolution within the thin shear band, a scaling factor ξ defined as the ratio between mesh size L_e and shear band thickness e is adopted to scale the heat and pore pressure related parameters. In this way, the equations related to temperature and pore pressure (mass and energy conservation) can be deemed as being solved on a scaled grid (centimetre scale, as the relevant parameters have been scaled), while the momentum balance equation governing mass sliding kinematics is solved on an unscaled grid (meter scale). The two sets of systems exchange frictional heat and pore pressure data via their shared contact nodes on the sliding surface.

2.3.1. Sliding kinematics

Within the explicit Generalized Interpolation Material Point method (GIMP) modelling framework (Bardenhagen and Kober, 2004), the momentum balance equation Eq. (10) is discretized in space and time, and solved first in each time step. At each active node, the acceleration at time t^n can be solved as:

$$\boldsymbol{a}_i^n = \frac{\boldsymbol{f}_i^n}{m_i^n} = \frac{\left(\sum_p S_{ip}^n m_p^n \boldsymbol{b} - \sum_p V_p^n \boldsymbol{\sigma}_p^n \cdot \boldsymbol{G}_{ip}^n\right)}{m_i^n} \tag{12}$$

where S_{ip}^n is the GIMP shape function, with $\boldsymbol{G}_{ip}^n$ being its gradient; V_p^n is the particle volume of an arbitrary material point p; m_i^n is the nodal mass

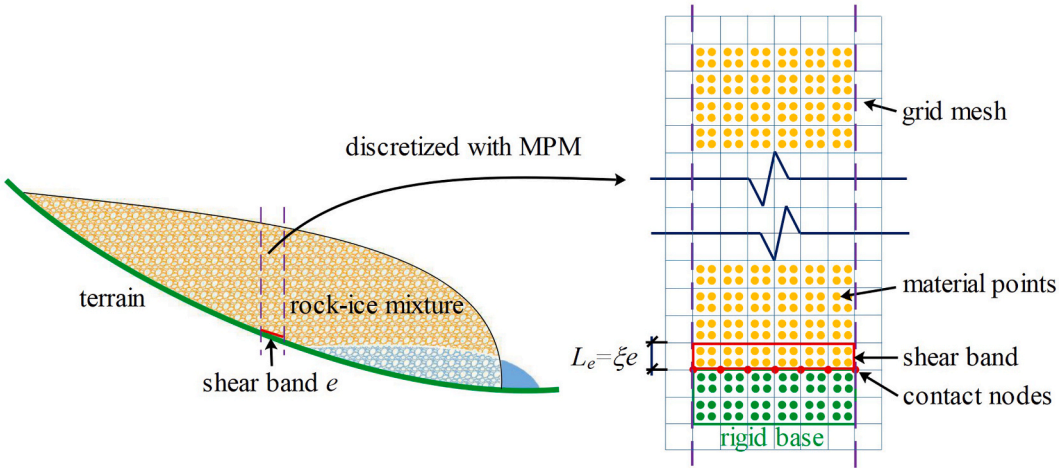

Fig. 2. MPM representation of the rock-ice mixture sliding on a rigid terrain.

of an arbitrary node i, calculated by $m_i^n = \sum_p S_{ip}^n m_p^n$.

The particle velocity $\boldsymbol{v}_p^{n+1}$ and displacements $\boldsymbol{x}_p^{n+1}$ at time t^{n+1} is updated with the FLuid Implicit Particle (FLIP) scheme (Brackbill, 1988; Lei et al., 2021b):

$$\boldsymbol{v}_p^{n+1} = \boldsymbol{v}_p^n + \sum_i \boldsymbol{a}_i^n S_{ip}^n \Delta t \tag{13}$$

$$\boldsymbol{x}_p^{n+1} = \boldsymbol{x}_p^n + \boldsymbol{v}_i^n S_{ip}^n \Delta t + \frac{1}{2}\boldsymbol{a}_i^n S_{ip}^n (\Delta t)^2 \tag{14}$$

Within the multi-material MPM contact modelling framework, the nodal momenta and forces of the contacting materials should be modified to reflect the implemented contact mechanics (Nairn, 2013). As the basal terrain is treated as a static rigid material, its momentum (velocity) cannot be changed, but it can exert forces on the landslide particles through contact (Lei et al., 2024). The momenta $\boldsymbol{P}_i^n$ and forces $\boldsymbol{f}_i^n$ for those contact nodes associated with the sliding mass should be corrected by the contact mechanism:

$$\boldsymbol{P}_i^{n'} = \boldsymbol{P}_i^n + \Delta \boldsymbol{P}_i^{n'}; \quad \boldsymbol{f}_i^{n'} = \boldsymbol{f}_i^n + \frac{\Delta \boldsymbol{P}_i^{n'}}{\Delta t} \tag{15}$$

In the above equation, $\boldsymbol{P}_i^{n'}$ and $\boldsymbol{f}_i^{n'}$ are the corrected momenta and forces of the slide mixture after doing contact. $\Delta \boldsymbol{P}_i^{n'}$ is the associated momentum change due to contact, which can be calculated according to their kinematic states (Nairn, 2013).

$$\begin{aligned} &stick: \quad \Delta \boldsymbol{P}_i^{n'} = \left(-N_i^n A_i^n \Delta t\right)\boldsymbol{n} + \left(S_i^{\text{stick},n} A_i^n \Delta t\right)\boldsymbol{t} \\ &slide: \quad \Delta \boldsymbol{P}_i^{n'} = \left(-N_i^n A_i^n \Delta t\right)\boldsymbol{n} + \left(S_i^{\text{slide},n} A_i^n \Delta t\right)\boldsymbol{t} \end{aligned} \tag{16}$$

where $\boldsymbol{n}$ and $\boldsymbol{t}$ are the normal and tangential vectors on the contact node i. For the stick condition, the contacting materials should move in a single velocity field with their centre-of-mass velocity. The normal compression N_i^n and the tangential stick traction $S_i^{\text{stick},n}$ can be calculated with $N_i^n = \boldsymbol{P}_i^n \cdot \boldsymbol{n} / \left(A_i^n \Delta t\right)$ and $S_i^{\text{stick},n} = -\boldsymbol{P}_i^n \cdot \boldsymbol{t} / \left(A_i^n \Delta t\right)$ accordingly, with A_i^n being the contact area (Nairn, 2013). For the sliding condition, the sliding surface would slide with a tangential sliding force S_i^{slide} lower than the stick traction S_i^{stick}, which is classically calculated by the Coulomb friction law. In this work, a more generalized Coulomb friction law which takes into account the contributions of adhesion strength and excess pore pressure is adopted to calculate the tangential sliding force.

$$S_i^{\text{slide},n} = \mu_S^e \left(N_i^n - P_{pore,i}^n\right) + c_S \tag{17}$$

where μ_S^e is the effective friction coefficient; c_S is the cohesion along the sliding surface; $P_{pore,i}^n$ is the pore pressure associated with node i.

2.3.2. Temperature evolution

As for the temperature evolution, the energy conservation equation Eq.(9) is discretized with the classic linear MPM shape functions and solved explicitly with the FLIP scheme. The temperature field associated with each material point at the end of each step is updated with:

$$T_p^{n+1} = T_p^n + \sum_i a_{T,i}^n \overline{S}_{ip}^n \Delta t \tag{18}$$

where the nodal change rate of temperature a_{Ti}^n is solved on the background grid with:

$$a_{T,i}^n = \frac{\sum_p V_p^n \left[\left(-\xi k_{Tm} \nabla T_p^n\right)\cdot \overline{\boldsymbol{G}}_{ip}^n + q_{s,p}^n \overline{S}_{ip}^n - \rho_L C_L \left(-\xi \frac{k_L}{\gamma_L} \nabla P_p^n\right)\cdot \nabla T_p^n \overline{S}_{ip}^n\right]}{\sum_p \overline{S}_{ip}^n \left[\sum_{\alpha=S,L,I} \boldsymbol{n}_{\alpha,p} \rho_\alpha C_\alpha + \rho_I n_p L_f \left(\frac{\partial S_L}{\partial T}\right)_p^n\right] V_p^n \Big/ \xi} \tag{19}$$

Note that the classic linear shape functions $\overline{S}_{ip}^n$ and their gradients $\overline{\boldsymbol{G}}_{ip}^n$ are adopted (instead of the GIMP shape functions) for a better representation of thermal evolution within the shear band (Lei et al., 2024).

In this work, the heat source is assumed only related to the frictional heating on the contact nodes. Accordingly, the heat source term $\sum_p V_p^n q_{sp}^n \overline{S}_{ip}^n$ in the above equation can be replaced with the frictional heating rate $q_{s,i}^n$ for those contact nodes, which is calculated within the multi-material contact framework as (Nairn et al., 2018):

$$\begin{aligned} q_{s,i}^n &= \frac{\int_0^{\Delta t} \left(S_i^{\text{slide},n} A_i^n \boldsymbol{t}\right)\cdot \left[\frac{\left(S_i^{\text{stick},n} - S_i^{\text{slide},n}\right) A_i^n \Delta t}{m_i^n} \boldsymbol{t}\right] dt}{\Delta t} \\ &\approx \frac{S_i^{\text{slide},n}\left(S_i^{\text{stick},n} - S_i^{\text{slide},n}\right)\left(A_i^n\right)^2 \Delta t}{m_i^n} \end{aligned} \tag{20}$$

where both the tangential frictional force $S_i^{\text{slide},n} A_i^n \boldsymbol{t}$ and the sliding velocity $\left(S_i^{\text{stick},n} - S_i^{\text{slide},n}\right) A_i^n \Delta t / m_i^n \boldsymbol{t}$ are assumed to be constant during each time step Δt.

2.3.3. Pore pressure evolution

The nodal pore pressure $P_{pore,i}^n$ in Eq. (17) is calculated from:

$$P_{pore,i}^n = \sum_p \overline{S}_{ip}^n \left[S_{L,p}^n P_{L,p}^n + \left(1 - S_{L,p}^n\right) P_{I,p}^n\right] \tag{21}$$

In the above equation, the saturation $S_{L,p}^n$ associated with each particle is linked to the corresponding particle temperature $T_{L,p}^n$ through a specific soil freezing characteristic curve, *i.e.* $S_{L,p}^n = f\left(T_{L,p}^n\right)$. At the initial stage, the pore structure is mainly filled by ice. Following He et al. (2023), the pore ice pressure is estimated with $P_{I,p}^n = \rho_I g H_p^n$ (with H_p^n being the flow depth of the particle). When both liquid and ice coexist in the pore ($0 < S_{L,p}^n < 1$), the pore liquid pressure is assumed can be estimated based on the pore ice pressure via the Clapeyron equation Eq.(4); once the ice has been fully melt, the pore liquid pressure is calculated based on mass conservation equations, which is updated with:

$$P_{L,p}^{n+1} = P_{L,p}^n + \sum_i a_{P,i}^n \overline{S}_{ip}^n \Delta t \tag{22}$$

where the nodal change rate of pore liquid pressure $a_{P,i}^n$ is derived from Eq.(8). By neglecting the pore liquid pressure contribution related to the skeleton deformation, the nodal pore liquid pressure change rate can be written as:

$$a_{P,i}^n = \frac{K_L \left\{\sum_p V_p^n \left(-\xi \frac{k_L}{\gamma_L} \nabla P_p^n\right)\cdot \overline{\boldsymbol{G}}_{ip}^n + \sum_p V_p^n \left[\beta_{m,p}^n - \left(1 - \frac{\rho_I}{\rho_L}\right) n_p^n \left(\frac{\partial S_L}{\partial T}\right)_p^n\right]\left(\frac{\partial T}{\partial t}\right)_p^n \overline{S}_{ip}^n\right\}}{n_p^n S_{L,p}^n \sum_p V_p^n \overline{S}_{ip}^n} \tag{23}$$

with the volumetric thermal expansion coefficient $\beta_{m,p}^n$ being calculated

from $\beta_{m,p}^n = \left(1-n_p^n\right)\left[S_{L,p}^n + \left(1-S_{L,p}^n\right)\frac{\rho_L}{\rho_L}\right]\beta_S + n_p^n S_{L,p}^n \beta_L + n_p^n\left(1-S_{L,p}^n\right)\frac{\rho_L}{\rho_L}\beta_I$.

3. Numerical examples

As mentioned, the proposed MPM framework comprises two key components. The first component mainly deals with the ice-water phase change within the shear band due to elevated temperature along with the sliding of the rock-ice mixture. The second component mainly models the frictional heating-induced thermal pressurization phenomenon, whereby the frictional work generated along the sliding surface is converted into heat, triggering both thawing and thermal pressurization processes within the basal shear band. In this section, three examples under two-dimensional plane strain conditions are presented to demonstrate the validity and capability of the proposed MPM framework. Firstly, the ice-water phase change modelling component is validated against analytical solutions, with which the influence of soil freezing characteristic curve (SFCC) and latent heat coefficient is demonstrated. Subsequently, the frictional heating process in a saturated frozen porous medium is simulated to demonstrate the effect of shear band thickness. Finally, the runout behaviour of an elastoplastic rock-ice mixture sliding on an inclined rigid plane is investigated, focusing on the interactions among different hypermobility mechanisms.

3.1. Freezing of a semi-infinite porous medium

The proposed MPM framework is first benchmarked by simulating the freezing process in a semi-infinite porous medium, as described in McKenzie et al. (2007). In our MPM simulations, this semi-infinite medium is represented by a 2 m long porous bar (Fig. 3), which is discretized with a mesh of square elements with the size of 0.01 m and 4 particles per cell (PPC). The porous bar is initially unfrozen with a uniform temperature of 0 °C. A subfreezing temperature of −3 °C is applied to the left boundary to initiate the freezing process along the bar.

The model parameters are adopted from McKenzie et al. (2007), which are summarized as: intrinsic density of soil grains $\rho_S = 2600$ kg/m^3, intrinsic density of water $\rho_L = 1000$ kg/m^3, intrinsic density of ice $\rho_I = 920$ kg/m^3, porosity $n = 0.95$, specific heat capacities of soil grains $C_S = 840$ J/kg, specific heat capacities of water $C_L = 4187$ J/kg, specific heat capacities of ice $C_I = 2108$ J/kg, latent heat coefficient of water $L_f = 333.5 \times 10^3$ J/kg, thermal conductivity of soil grains $k_{TS} = 2.9$ W/(m°C), thermal conductivity of water $k_{TL} = 0.58$ W/(m°C), thermal conductivity of ice $k_{TI} = 2.14$ W/(m°C). In these simulations, the total simulation time is set to 1 day, with a time step of 1×10^{-4} days. The thermal conductivities of each phase are scaled by a factor of 86,400 (seconds per day) accordingly. Note that a high porosity $n = 0.95$ was adopted from McKenzie et al. (2007) for validation consistency, accounting possible extreme conditions.

In this example, the sensitivity of the freezing function's shape and the latent heat was evaluated using the linear freezing function $S_L = mT + 1$ $(0 \le S_L \le 1)$ for four parameter sets: $m = 0.25$ (MPM-m0.25), $m = 0.5$ (MPM-m0.5), $m = 1.0$ (MPM-m1), and $m = 0.5$ without latent heat (MPM-m0.5-L0). As shown in Fig. 4, the temperature and saturation profiles obtained at the end of the simulations in this study closely match the corresponding FEM results from McKenzie et al. (2007). Over time, the applied subfreezing temperature propagates along the bar (Fig. 4a), causing the soil to freeze from the left end (Fig. 4b). Using a steep freezing function (large m) produces a narrow freezing front with a small distance between the fully frozen and thawed regions. Meanwhile, the release of latent heat ($L_f \neq 0$) slows the progression of the freezing front and creates a steeper temperature gradient between these regions.

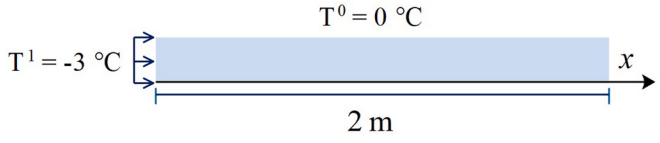

Fig. 3. Initial and boundary conditions of the porous bar.

3.2. Elastic rock-ice block sliding with controlled velocity

The MPM framework's ability to model frictional heating-induced thermal pressurization in saturated unfrozen soils has been validated against analytical solutions in Lei et al. (2024). In this section, the same sliding block problem is investigated, but with the unfrozen soil block replaced by a rock-ice mixture block. As shown in Fig. 5, a frozen rock-ice block, 100 m long and 50 m high, with an initial temperature of −10°C is considered. Two rigid frames are imposed as boundary constraints to drive the block to slide at a constant horizontal velocity of 1 m/s along a rigid plane, initiating the frictional heating-induced thermal pressurization process within the rock-ice mixture under a gravitational acceleration of g = 9.81 m/s^2. By default, the cell size is chosen as 10 m × 10 m with 4 PPC ($L_e = 10$ m), and the time step is set to 1×10^{-3} s.

In this example, to minimize skeleton deformation, the rock-ice mixture is modeled as a thermo-poro-elastic medium with a Young's modulus E of 1 GPa and a Poisson's ratio υ of 0. The friction coefficient between the rock-ice mixture and the rigid plane is set to 0.2. The thermal and physical properties of the constituents in the rock-ice mixture were adopted from He et al. (2023) and are presented in Table 1. There are numerous functions used to describe the relationship between unfrozen water content and temperature in frozen soils. According to He et al. (2023), the following experimentally derived fitting curve is adopted to describe the soil freezing characteristic curve (SFCC) of the rock-ice mixture.

$$S_L = \begin{cases} \left[1 - \left(T - T_{ref}\right)\right]^{-5} & T < T_{ref} \\ 1 & T \ge T_{ref} \end{cases} \tag{24}$$

where T_{ref} is the thawing point of ice, which is set to 0 °C.

Shear band thickness is a key parameter in the proposed model for controlling the thermal pressurization process. Fig. 6 compares the evolution profiles of average temperature, saturation, and pore pressure within shear bands corresponding to three different thickness values ($e = 0.05$ m, 0.1 m, 0.2 m), assuming zero conduction and permeability. Under constant friction velocity, the same amount of frictional work leads to a higher temperature in a thinner shear band, resulting in a stronger thermal pressurization effect within the shear band (Lei et al., 2024). As Fig. 6a illustrates, the average temperature rises at a higher rate in thinner shear bands. Consequently, this results in a commensurately faster rise in the average liquid saturation (Fig. 6b), according to the SFCC curve Eq.(24).

Following He et al. (2023), the local pore pressure is calculated as an averaged value of the pore ice pressure and the pore liquid pressure, $P_{pore} = S_L P_L + (1 - S_L) P_I$ (as presented by Eq.(21)). During the initial phase of thawing, both water and ice coexist in local pores. The increase in liquid saturation S_L reduces the relative contribution of pore ice pressure ($P_I = \rho_I g H$, representing hydrostatic ice pressure under gravity). Simultaneously, the pore liquid pressure P_L declines as pore ice thaws, in accordance with the Clapeyron equation Eq.(4). Together, these effects cause the overall pore pressure to decrease progressively during the initial thawing stage (Fig. 6c). Once a material point fully melts, its pore pressure is updated using the pore liquid pressure equation Eq.(8). As thawing propagates through the shear band with increasing numbers of material points reaching the thawing temperature T_{ref}, the domain-averaged pore pressure exhibits a gradual increase. Following this, the shear band transitions into a stage of rapid pressure buildup, as complete ice melting triggers a sharp pressure surge driven

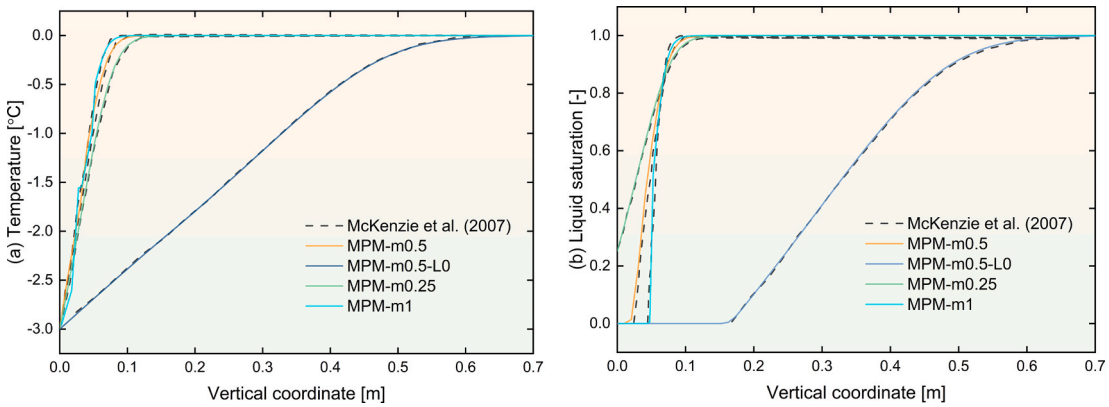

Fig. 4. Profiles of (a) temperature and (b) liquid saturation with four sets of SFCC parameters.

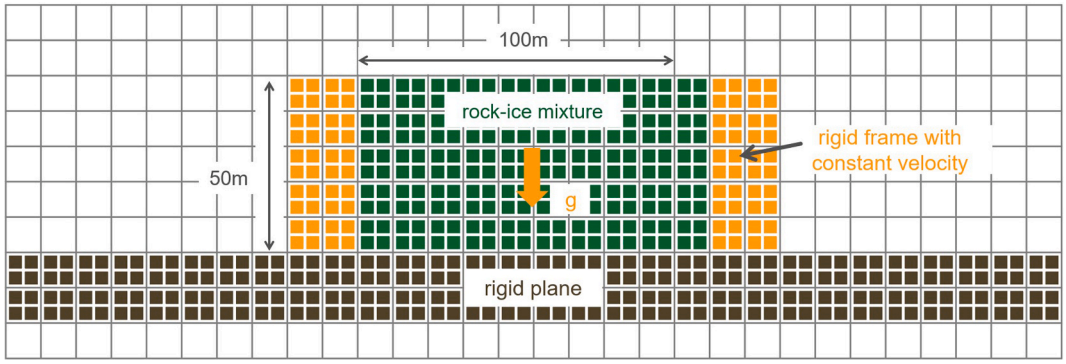

Fig. 5. MPM representation of the sliding block with imposed constant velocity.

Table 1
Thermal and physical parameters of the rock-ice mixture.

Parameters	Value	Parameters	Value
Density of water ρ_L [kg/m^3]	1000	Specific heat of rock grains C_S [J/(kg°C)]	858
Density of ice ρ_I [kg/m^3]	917	Specific heat of water C_L [J/(kg°C)]	4180
Density of rock grains ρ_S [kg/m^3]	2750	Specific heat of ice C_I [J/(kg°C)]	2040
Bulk modulus of liquid K_L [Pa]	1.0×10^9	Thermal conductivity of rock grains k_{TS} [W/(m°C)]	3.0
Thermal expansion coefficient of rock grains β_S [/°C]	3.0×10^{-5}	Thermal conductivity of liquid k_{TL} [W/(m°C)]	0.58
Thermal expansion coefficient of liquid β_L [/°C]	2.75×10^{-4}	Thermal conductivity of ice k_{TI} [W/(m°C)]	2.22
Thermal expansion coefficient of ice β_I [/°C]	5.1×10^{-5}	Latent heat of water L_f [J/m^3]	333.5×10^3

by the thermal pressurization mechanism. The increase in pore pressure would counteract some of the normal compression (Eq. (17)), which in turn reduces the generation of frictional heating according to Eq. (20). Consequently, both the average temperature and pore pressure profiles will achieve a relative equilibrium state. To evaluate the mesh sensitivity of the model, the numerical results obtained using cell sizes of $L_e = 5$ m, 10 m and 20 m, with a shear band thickness of $e = 0.1$ m, are also compared in Fig. 6. As can be seen, the results obtained with different cell sizes, but the same shear band thickness show good agreement with each other.

The hydraulic permeability of shear band soils is also an important parameter for the thermal pressurization effect. Fig. 7 compares the average temperature and pore pressure profiles for a shear band thickness of $e = 0.05$ m, obtained using four different hydraulic permeabilities: $k_L = 0$, 1×10^{-10} m/s, 1×10^{-9} m/s, and 1×10^{-8} m/s (indicated as KL0, KL10, KL9, KL8). By default, the thermal conduction parameters are set to the values in Table 1 (corresponding to the cases indicated with KT). For scenarios with zero permeability, we also investigated another case with zero thermal conduction (indicated with KT0). The comparison of cases with and without thermal conduction demonstrates that it has a negligible influence on the temperature and pore pressure profiles within the shear band during such a short duration. On the other hand, these evolution profiles are distinct under different sets of hydraulic permeabilities. It should be noted that all these saturation profiles closely match that of the case 'Le10m-e0.05′ shown in Fig. 6b. According to our model, excess pore liquid pressure will dissipate into the surrounding mass at a rate controlled by hydraulic permeability (via (Eq.(8)). As shown, a larger permeability leads to lower pore pressure accumulation after approximately 5 s (time corresponding to the complete melting of pore ice within the shear band). In contrast, a higher basal temperature is observed in scenarios with greater permeabilities. This phenomenon is attributed to the reduced pore pressures, which in turn increase tangential sliding forces and, consequently, the frictional heating rate.

3.3. Elastoplastic rock-ice mixture sliding on inclined surface

In this example, the runout kinematics of an elastoplastic rock-ice mixture sliding on an inclined rigid plane are investigated using the proposed THM-coupled MPM model. As shown in Fig. 8, the inclined

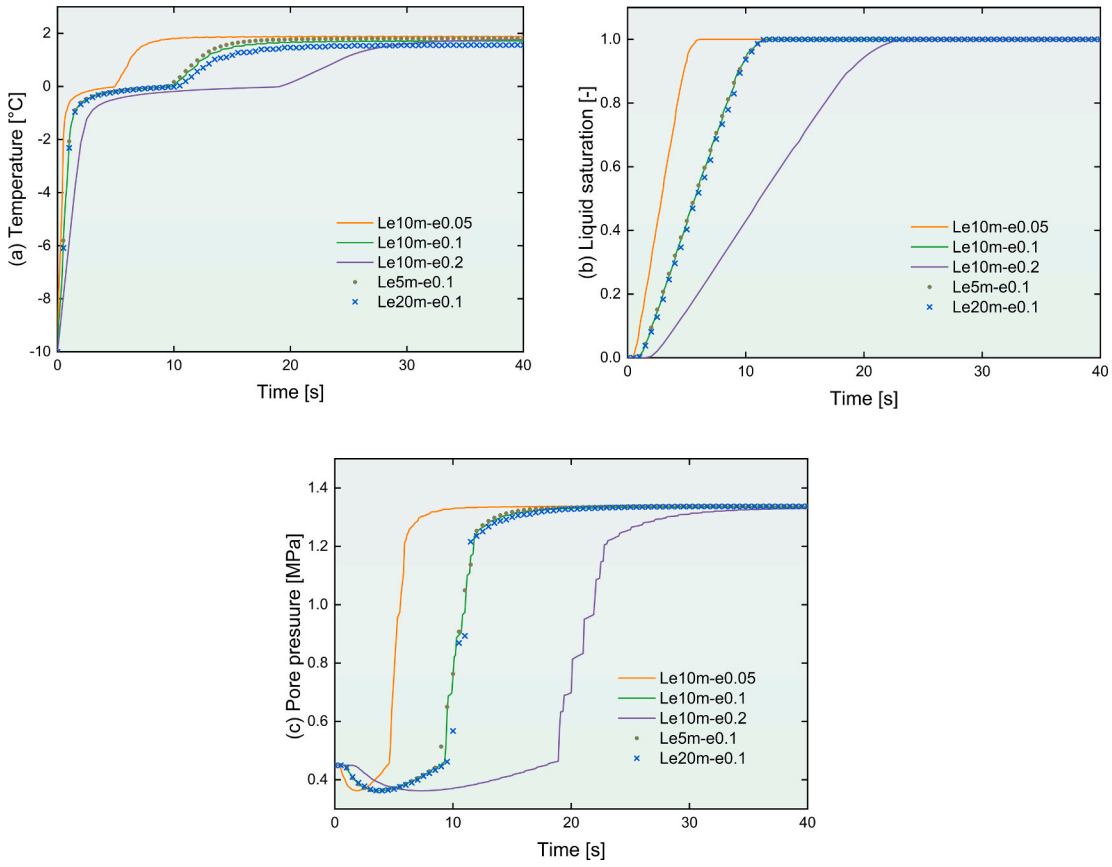

Fig. 6. Evolution profiles of (a) temperature, (b) saturation, and (c) pore pressure within shear bands of different thicknesses.

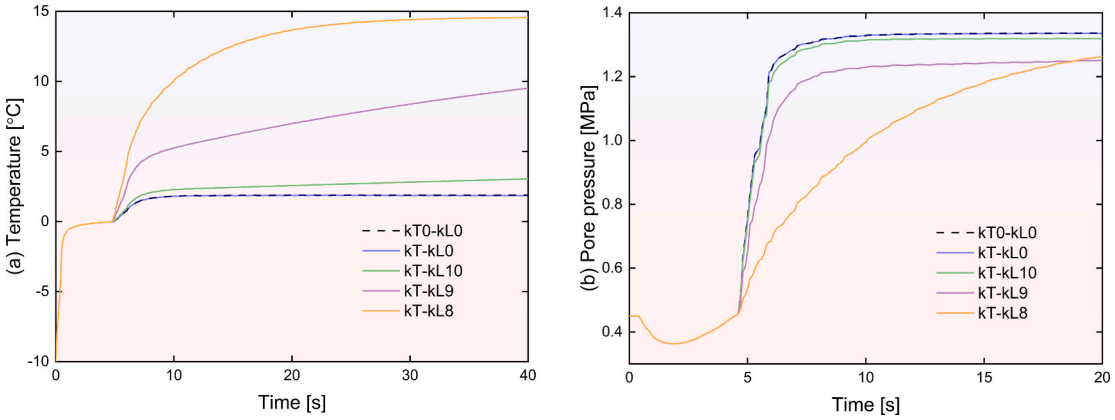

Fig. 7. Effect of permeability on the evolution of (a) temperature and (b) saturation within the shear band (e = 0.05).

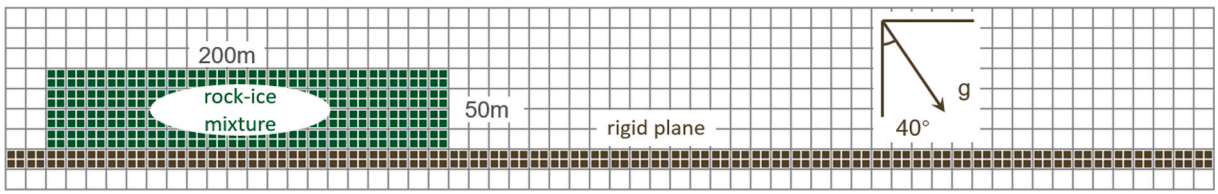

Fig. 8. MPM representation of the rock-ice mixture sliding on an inclined surface.

plane in the MPM model is represented by two layers of horizontally distributed material points, subjected to a 40° anticlockwise-rotated gravity acceleration. Initially, a 200 m long, 50 m high frozen rock-ice block is positioned on the inclined surface. Under gravity, the rock-ice block slides along the inclined plane, triggering a series of THM-coupled processes that, in turn, affect its runout kinematics.

In reality, the sliding rock-ice mixture would experience intense fragmentation and deformation during the runout process. In this example, the block is simulated as an isotropic thermo-poro-elastoplastic medium by default. The Mohr-Coulomb failure criterion Eq.(11) is adopted to account for the plastic failure of the mixture. Besides the thermal pressurization mechanism illustrated in Section 3.2, the meltwater would internally reduce the friction between the solid particles, thus further lubricates the sliding surface. The modified Coulomb friction law Eq.(17) is used to simulate the frictional contact between the slider and the basal terrain. To account for the variation of ice fraction along the sliding surface, the following effect basal friction angle μ_S^e (Pudasaini and Krautblatter, 2014) is adopted to replace the constant basal friction angle μ_S, in which a lubrication factor L_ϕ is introduced to reduce the basal friction angle μ_S based on the effective solid volume fraction n_S^e (defined by Eq. (2)).

$$\mu_S^e = L_\phi(n, S_L)\mu_S = \left[1 - \left(1 - \frac{n_S^e - n_{Smin}^e}{n_{Smax}^e - n_{Smin}^e}\right)^\omega\right] tan\varphi_f \tag{25}$$

where $\omega = 2$ governs the fluidization exponent (He et al., 2023), n_S^e is updated from shear band saturation, and φ_f is the initial basal friction angel. n_{Smin}^e, n_{Smax}^e are the minimum and maximum values of the effective solid volume fraction, being chosen as 0.05 ($n = 0.95$, $S_L = 1$) and 0.85 ($n = 0.225$, $S_L = 0$) respectively.

In this example, the environmental temperature is set to −10°C. The thermal and physical parameters of the rock-ice mixture are taken from Table 1 (refers to He et al. (2023)), and the hydromechanical parameters are provided in Table 2 (refers to Pudasaini and Krautblatter (2014)). The initial shear band thickness is set to 0.05 m. To account for the energy transfer other than frictional heat (Pudasaini and Krautblatter, 2014; He et al., 2023), an energy conversion coefficient of 0.35 is introduced to reduce the frictional heating rate (*i.e.*, the heating source term in Eq. (19) is replaced with 0.35 $q_{s,i}^n$ for those contact nodes). The cell size is chosen as 5 m × 5 m with 4 PPC, and the time step is set to 1.0×10^{-3} s.

Four scenarios, each with a different combination of the three distinct hypermobility mechanisms—internal plastic deformation (D), basal lubrication (L), and thermal pressurization (P)—are simulated. For cases with plastic deformation, we simulated the mixture using the elastoplastic model with Mohr-Columb yield function Eq. (11); otherwise, its elastic component is used. For cases with basal lubrication, the lubrication factor L_ϕ for each contacting node is calculated using updated saturation and porosity values extrapolated from the material points in the shear band; otherwise, the initial saturation and porosity are used (Eq. (25)). For cases with thermal pressurization, the nodal pore pressures used to calculate the tangential sliding forces (Eq. (17)) are updated using the pore pressure evolution equation Eq. (21); otherwise, the pore pressures of these contact nodes are set to zero directly. The evolution profiles of the average temperature and liquid saturation within the shear band, corresponding to these scenarios, are plotted in Fig. 9. Meanwhile, Fig. 10 presents the evolution profiles of the average effective friction coefficient along the basal frictional surface, the average pore pressure within the shear band, and the average equivalent plastic strain within the rock-ice mixture. Further, the corresponding global velocity and displacement profiles of the entire rock-ice mixture for these cases are presented in Fig. 10.

Table 2
Hydromechanical parameters of the sliding block.

Parameters	Value	Parameters	Value
Young's modulus E [Pa]	5.0×10^8	Initial basal friction angel φ_f [∘]	40
Possion's ratio υ [-]	0.2	Cohesion strength of the contact surface c_S [kPa]	0
Initial porosity n [-]	0.375	Initial internal friction angel φ [∘]	35
Hydraulic conductivity k_L [m/s]	1.0×10^{-9}	Internal cohesion c [kPa]	250

During the rapid frictional sliding process, the basal temperature in all cases increases gradually due to frictional heating (Fig. 9a), which melts the ice inside the shear band over time (Fig. 9b). For Case D, although the frictional heating and ice thawing processes have been simulated, their influence on the basal frictional force was ignored by setting a constant friction coefficient and zero pore pressure (Fig. 10). This case represents a scenario without any THM-coupled effect and exhibits the lowest kinematic characteristics among all cases, as shown in Fig. 11. In Case D-L, the friction coefficient is modelled as a function of porosity and liquid saturation, which decreases commensurate with skeleton deformation and ice melting (Fig. 10a). Relative to Case D, the diminished friction coefficient in Case D-L leads to a marginally increased sliding velocity and accelerated frictional heating.

When thermal pressurization is further accounted for (Case D-L-P), the pore pressure generated within the shear band can counterbalance part of the normal pressure (Fig. 10b). This significantly increases the runout velocity of the mixture compared to cases without thermal pressurization (Fig. 11b). Initially, the faster basal frictional velocity in this case accelerates the frictional melting process (before around t = 15 s). Later, the gradually increasing excess pore liquid pressure significantly decreases the basal frictional force, which in turn reduces the frictional heating rate (temperature increase rate) in the shear band (Fig. 9). Furthermore, due to the lower basal frictional force, the internal plastic deformation in this case is much lower than in cases without thermal pressurization (Fig. 11a), hence less friction decreases due to porosity change (Fig. 10a).

For comparison, we also present results for the case without plastic deformation (case P-L). In this scenario, the rock-ice mixture's yield strength is set to a high value to prevent any plastic deformation. Accordingly, the rock-ice block would largely retain its initial shape during the sliding process. This, in turn, leads to higher flow heights compared to cases with plastic deformation. Compared with Case D-P-L, the friction coefficient's behaviour in this case is largely governed by the rising liquid saturation in the shear band. After t = 10 s, when the ice within the shear band has completely melted, this saturation stabilizes at a relatively constant value (Fig. 10a). Additionally, the greater flow height produces more frictional work, which in turn results in a more intense frictional heating process (Fig. 9) and a correspondingly higher basal excess pore pressure evolution profile (Fig. 10b). In Fig. 11b, the average velocity in this case develops slightly slower than in Case D-P-L during the initial stage, where the thermal pressurization mechanism hasn't fully taken effect. Later, the profiles in both cases are almost parallel after approximately t = 10 s. This implies the dominant role of the thermal pressurization mechanism in facilitating the hypermobility of rock-ice advances.

4. THM-coupled simulation of the Lamplugh rock-ice avalanche

4.1. MPM model of the Lamplugh avalanche

In this section, the Lamplugh rock-ice avalanche is chosen as a case study to test the capability of our MPM simulation framework. This avalanche occurred in Glacier Bay National Park and Preserve (GBNP), southern Alaska, on June 28, 2016 (Fig. 12a). The elevation difference between pre- (June 15, 2016) and post-event (July 16, 2016) DEMs over the Lamplugh rock avalanche deposit was analyzed in detail by Bessette-Kirton et al. (2018) and is shown in Fig. 12b. Due to increased melting at higher altitudes and consequent permafrost degradation (Coe et al., 2018), the Lumplugh avalanche originated from a bedrock ridge at approximately 2,150 m asl (above sea level). The total source volume was estimated to be around 52 ± 2 million m^3 with an average thickness of 50.0 m. The avalanche then flowed through a mountain valley approximately 2,500 m wide, confined by steep mountains on both sides, and travelled a distance of approximately 10,500 m. The unimaginable long runout makes it difficult to explain within the classical

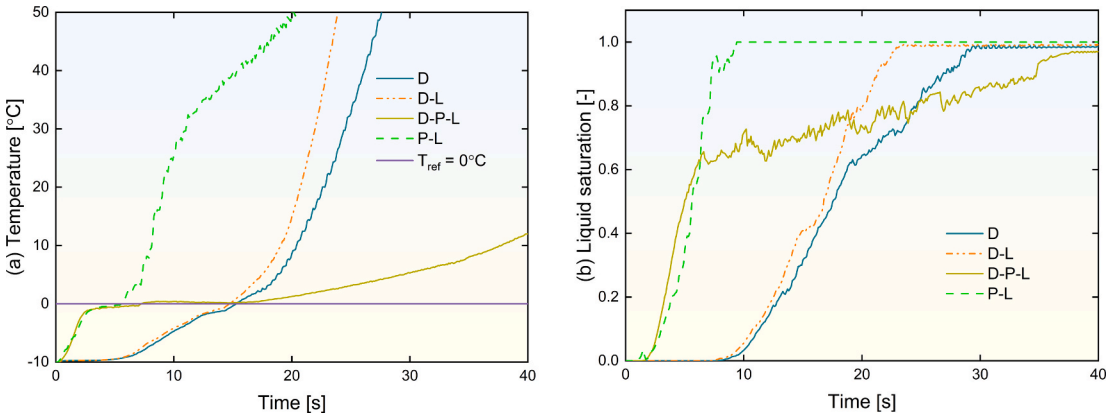

Fig. 9. Evolution profiles of (a) temperature and (b) liquid saturation within the shear band.

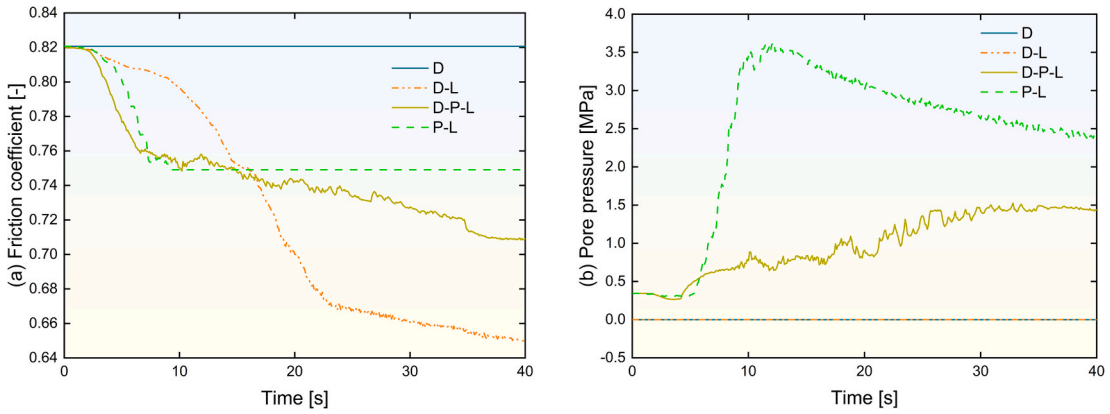

Fig. 10. Evolution profiles of (a) friction coefficient and (b) pore pressure along the sliding surface.

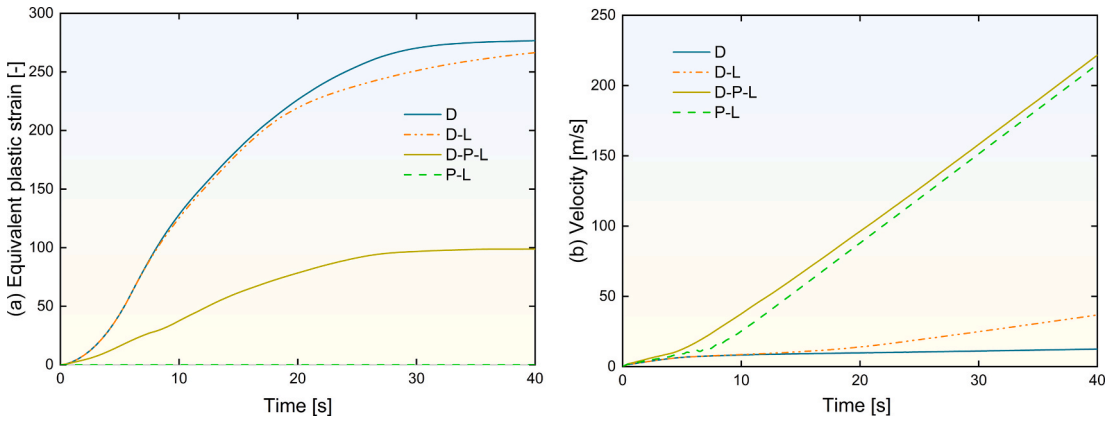

Fig. 11. Evolution profiles of (a) equivalent plastic strain and (b) velocity of the rock-ice mixture.

frictional framework (He et al., 2023).

In this example, we conduct a plane strain analysis of the Lumplugh rock-ice avalanche using the proposed THM-coupled MPM. The MPM model is constructed from the pre- and post-event elevation profiles through the avalanche's longitudinal cross-section L-L', as presented in Fig. 13. Based on the estimated source volume, the model's thickness is set to 60 m. As Bessette-Kirton et al. (2018) noted, the source region is uncertain due to blurry satellite images of the area. To facilitate our analysis, the source geometry adopted in our MPM model is slightly larger than the one calculated from the pre- and post-event elevation profiles (circled by red dots in Fig. 13). The source sliding material is represented by a set of particles modelled with thermo-poro-elastoplastic material, whereas the basal terrain is represented by rigid material points with thickness corresponding to three layers of elements. The interactions between rigid and non-rigid particles are governed by the multi-material contact model incorporating frictional heating. The background grid consists of 10 m $\times$ 10 m cells with 4 PPCs. The total number of particles is 12,716, of which 8,399 are non-rigid. The runout analysis is performed with a time step of 1×10^{-2} s for a total duration of 200 s. During this short simulation period, the sliding material is treated as adiabatically insulated from the surrounding air, while pore pressures at its surface remain at ambient atmospheric pressure (zero gauge).

The material parameters used to simulate the Lamplugh rock-ice avalanche are listed in Table 1 (thermal and physical parameters) and

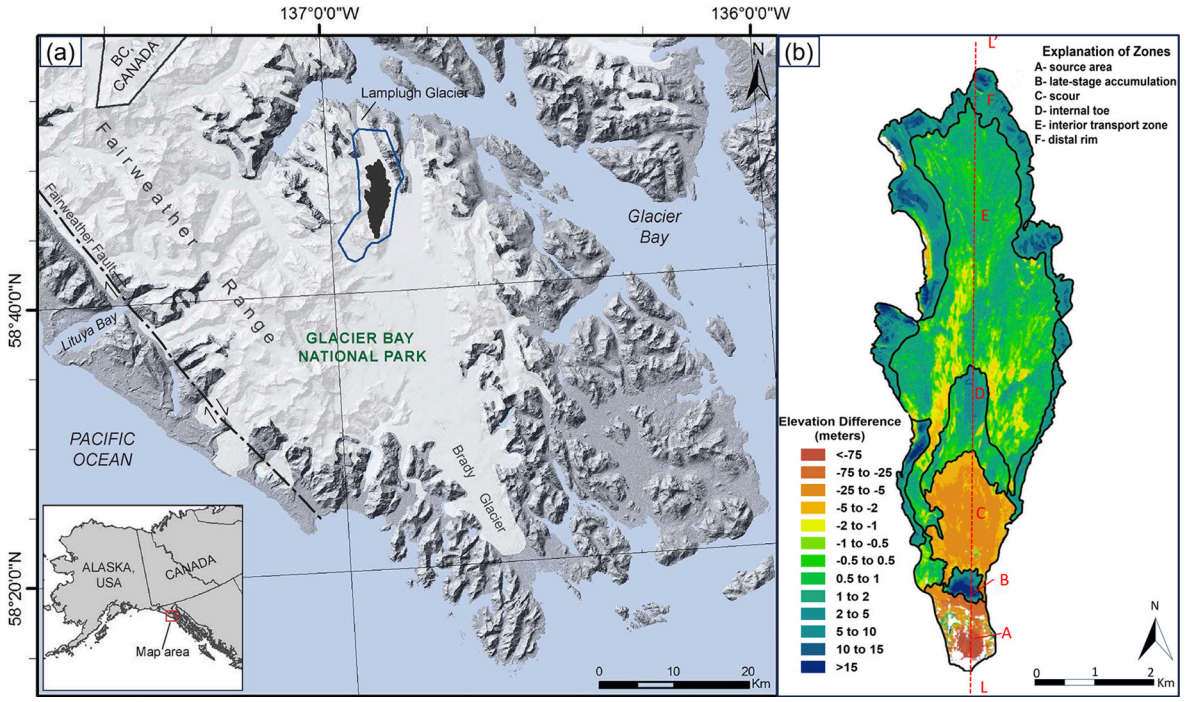

Fig. 12. Location (a) and elevation difference (b) of Lumplugh rock-ice avalanche (modified from Bessette-Kirton et al., 2018).

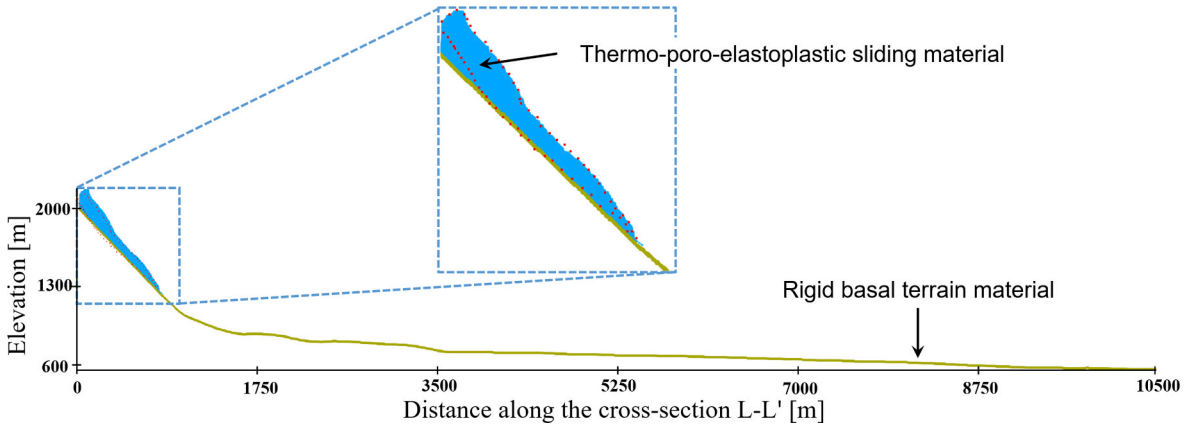

Fig. 13. MPM representation of the cross-section L-L' of Lumplugh rock-ice avalanche.

Table 3
Hydromechanical parameters for Lamplugh rock-ice avalanche.

Parameters	Value	Parameters	Value
Young's modulus E [Pa]	5.0×10^8	Initial basal friction angel φ_f [∘]	40
Possion's ratio υ [-]	0.2	Cohesion strength of the contact surface c_S [kPa]	600
Initial porosity n [-]	0.375	Initial internal friction angel φ [∘]	35
Hydraulic conductivity k_L [m/s]	2.0×10^{-8}	Initial, final internal cohesion c_0, c_f [kPa]	1000, 100

Table 3 (hydromechanical parameters). The hydrothermal parameters are primarily referenced from He et al. (2023), who investigated the same avalanche using a sliding block model. The mechanical parameters are mainly taken from Pudasaini and Krautblatter (2014) for general rock-ice mixture material. The strength of rock-ice depends strongly on the hydrostatic pressure and temperature state (Fish and Zaretsky, 1997). A initial basal cohesion of 0.561 MPa was set in He et al. (2023) for initial equilibrium in their sliding block model. In this work, the cohesion along the sliding surface c_S is set to 0.6 MPa. Further to reflect the fragmentation, the internal cohesion c of the rock-ice mixture decreases from its initial value $c_0 = 1.0$ MPa to its final value $c_f = 0.1$ MPa with the increase of equivalent plastic strain ε_{eqv} via the following strain softening law $c = c_f + (c_0 - c_f)\exp(-\varepsilon_{eqv})$.

The shear band thickness is a key parameter that controls the generation of basal temperature and the diffusion of excess pore liquid pressure. To reflect the significant rock and ice fragmentation after the sliding mass hits the ground surface, the shear band thickness is increased from an initial value of 0.05 m to 0.5 m after t = 75 s (the time of peak velocity). Following He et al. (2023), an energy conversion coefficient of 0.35 is introduced to reduce the frictional heating rate. It should be noted that rock-ice avalanches have complex components, and their material properties may vary spatially. Therefore, the material parameters adopted here are averaged values, which were best-fitted to the velocity profile derived from seismic signals (Fig. 16a, Dufresne et al., 2019) and the deposition characteristics (Fig. 12b, Bessette-Kirton et al., 2018).

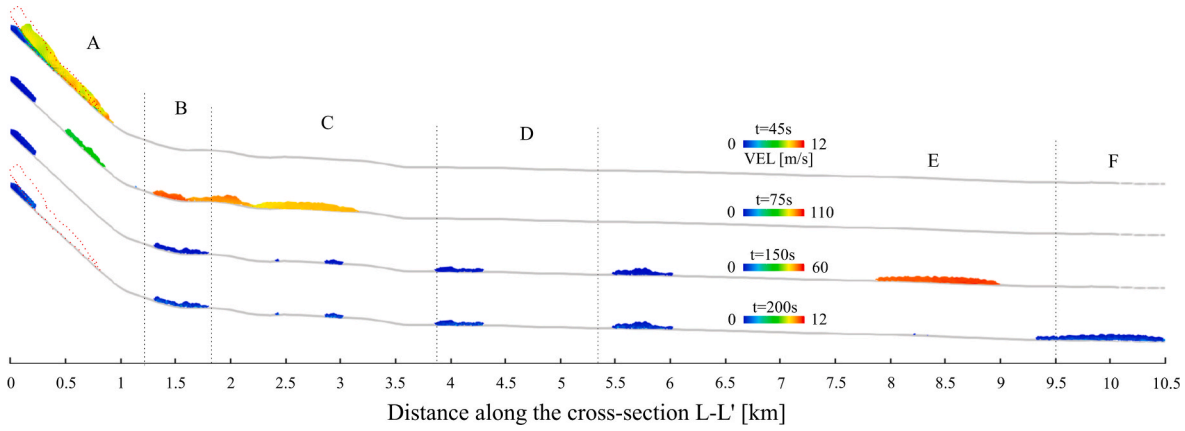

Fig. 14. Simulated velocity contours of the Lamplugh avalanche at different times.

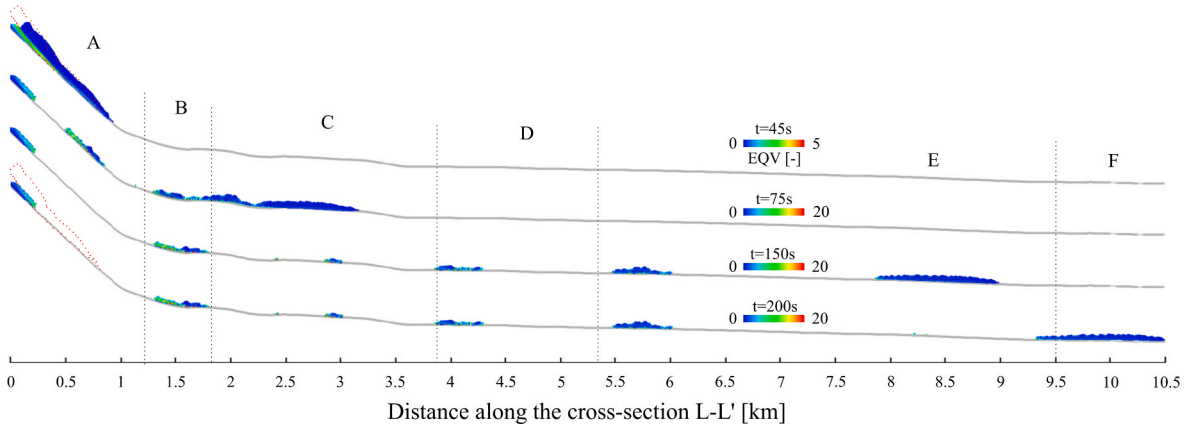

Fig. 15. Simulated equivalent plastic strain contours of the Lamplugh avalanche at different times.

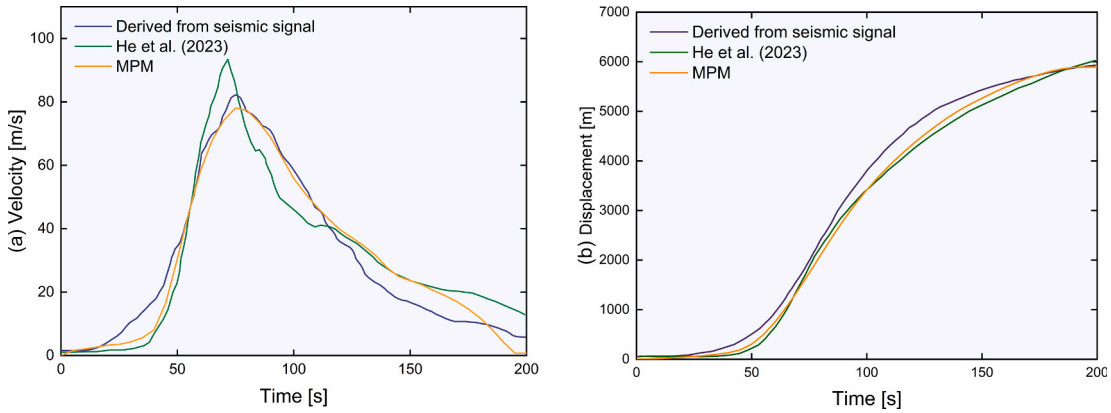

Fig. 16. Comparison of averaged (a) velocity and (b) displacement profiles obtained from MPM with results derived from seismic signal (Bessette-Kirton, 2016) and sliding block model (He et al., 2023).

4.2. THM-coupled avalanche dynamics

Fig. 14 and Fig. 15 presents the velocity and equivalent plastic strain contours at different times simulated by our THM-coupled MPM, in which zones with different elevation change characteristics are separated by the grey dot lines. Meanwhile, Fig. 16 compares the simulated runout velocity and distance profiles with those derived from seismic wave inversion by Dufresne et al. (2019), and with results obtained from the block model simulation of He et al. (2023). Consistent with field observations, the rock-ice mixture was initially positioned on the slope at approximately 2,150 m asl. When the simulation started, the slope underwent large shear deformation within its mass, given the specified material parameters. The simulated failure plane overlaps well with the post-failure surface (marked with red dots in contour figures). Prior to t = 40 s, the failed mass moved as a largely intact body along the slip surface. Subsequently, the failed mass dropped at an average slope of 48° to an elevation of approximately 900 m asl before sloping toward the surface of the Lamplugh Glacier at an average gradient of 8° (Bessette-Kirton et al., 2018). At this stage, the sliding body's potential energy rapidly converted into kinetic energy, with its speed quickly increasing

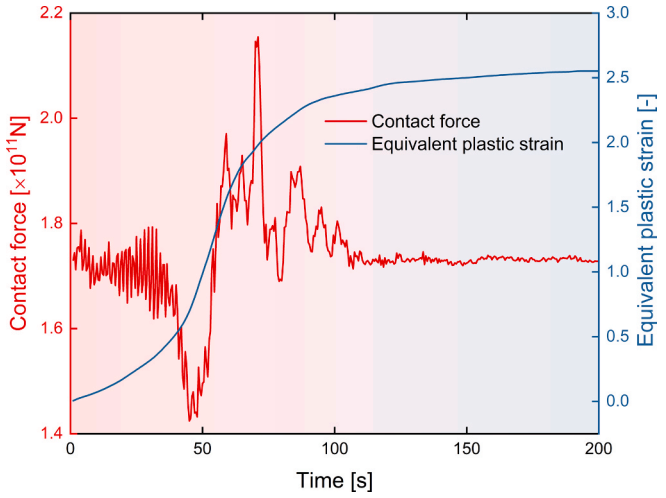

Fig. 17. Evolution profiles of the basal contact force and the equivalent plastic strain within the sliding mass.

from 8 m/s at t = 40 s to its peak of around 80 m/s at t = 75 s (Fig. 16). When the sliding mass hit the glacier surface with a gentle slope at around t = 75 s, strong interactions were observed on the contact surface (red line in Fig. 17). The magnitude of these interactions is comparable to the field impact force inverted from long-period seismic waves (a maximum inverted force of 2.8×10^{11} N as reported by Dufresne et al., 2019). Meanwhile, significant internal deformations occurred during this process (Fig. 15, light blue line in Fig. 17). As a result, the sliding mass broke into several blocks while moving across the valley floor with an average gradient of approximately 1.3° (Fig. 14). Due to frictional interactions with the valley surface, the failed mass then came to rest along the sliding path. As highlighted by the differenced DEM in Fig. 12b, significant material accumulation occurs in specific areas (Bessette-Kirton et al., 2018): just below the source (Zone B), in a toe-like feature in the middle of the deposit (Zone D), and along the lateral and distal margins (Zone F). Concurrently, a transport area (Zone E) contains regions of both accumulation and depletion. The simulated deposition characteristics demonstrated good concordance with the field data, with the exception of Zone C, as our model did not incorporate the erosion feature in that area.

As presented above, our MPM model accurately reproduces the average velocity and displacement of the sliding mass, as well as the deposition characteristics of the Lamplugh rock-ice avalanche. This demonstrates that the avalanche's extraordinarily long runout can be well explained by the THM-coupled mechanism. The simulated temperature and pore pressure contours at different times are presented in Fig. 18 and Fig. 19, respectively. Meanwhile, the evolution profiles of the THM-related field variables within the basal shear zone are displayed in Fig. 20. As shown, after the failed mass fully detaches from the bedrock ridge (t = 40 s), the temperature inside the basal shear zone (red line in Fig. 20a) increases rapidly with the frictional sliding process. This sharp temperature increase also leads to the rapid melting of ice within the shear zone. As the red line in Fig. 20b illustrates, the average liquid saturation within the shear zone rises from approximately 0.3 at t = 40 s to 0.9 at t = 75 s. The ice melting process decreases the effective solid volume fraction according to Eq.(25), which consequently leads to a direct reduction in the basal friction coefficient (light blue line in Fig. 20b). Furthermore, the average pore pressure increases sharply due to frictional heating. The resultant basal pore pressure accumulation directly reduces the effective frictional force along the sliding surface (Eq. (17)). This is the dominant mechanism contributing to the extraordinarily rapid velocity increase observed during this stage (between t = 40 s and 75 s). As stated by Campbell et al. (1995) and Zhao and Crosta (2018), the thickness of a landslide shear zone increases with intense shearing and increased basal roughness. In the simulation, after strong interactions with the ground surface, the shear band thickness is adjusted from an initial value of 0.05 m to 0.5 m at t = 75 s. Following this, the failed mass has travelled onto a much gentler ground surface. Consequently, the sliding velocity decreases gradually in conjunction with a slower frictional heating process. As depicted by the red line in Fig. 20a, the average basal temperature exhibits a gradual increase after t = 75 s (also evidenced by the temperature contours in Fig. 18). This suggests that the heat generation rate within the shear zone marginally exceeds the rate of heat diffusion into the surrounding rock mass. Meanwhile, the thermal pressurization process was overcome by pore pressure-diffusion, leading to a net decrease in pore pressure over time (Fig. 19). As a result, the velocity of the sliding mass decreases due to frictional contact along the valley surface, even with a reduced effective solid fraction and friction coefficient. By t = 200 s, the leading edge of the sliding mass had traversed approximately 10,500 m (Fig. 14). Meanwhile, the average sliding distance of the failed mass is around 5,612 m, which is slightly smaller than the derived value of 5,929 m shown in Fig. 16b.

5. Concluding remarks

This study introduces a novel Material Point Method (MPM) framework designed to model the thermo-hydro-mechanical (THM) coupled processes in rock-ice avalanches. The proposed framework integrates a THM-coupled three-phase single-point MPM formulation to effectively capture the complex interactions of skeleton deformation, pore water seepage, heat transfer, and ice-water phase transition within the sliding rock-ice mixture. Additionally, a multi-material MPM contact model is

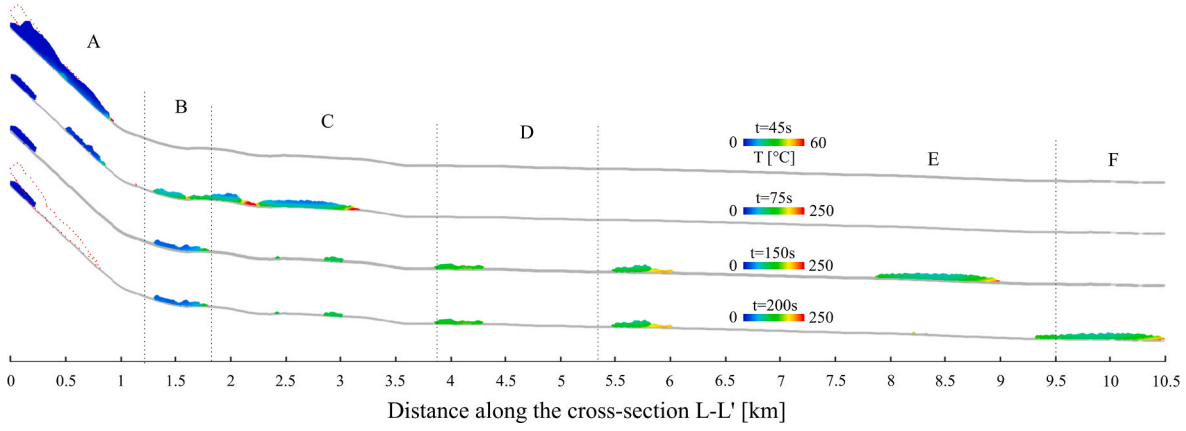

Fig. 18. Simulated temperature contours of the Lamplugh avalanche at different times.

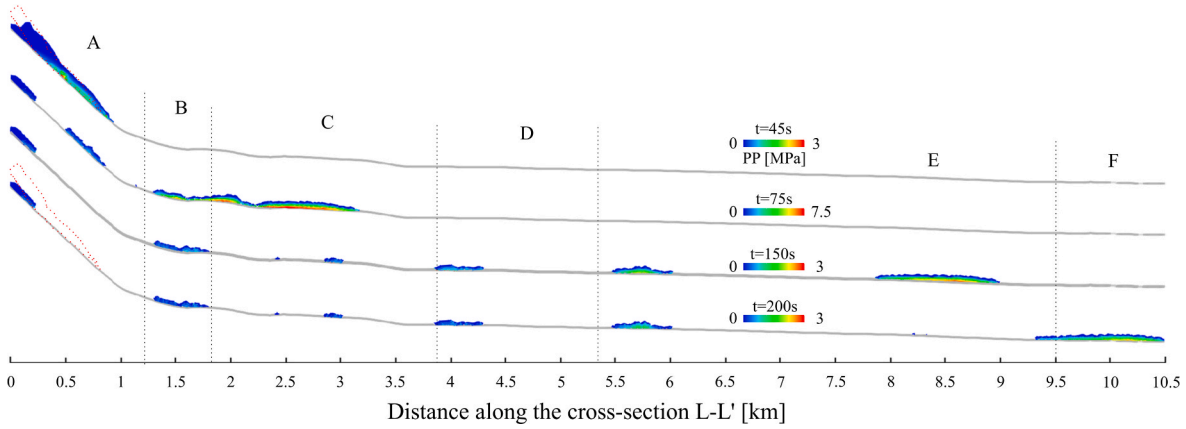

Fig. 19. Simulated pore pressure contours of the Lamplugh avalanche at different times.

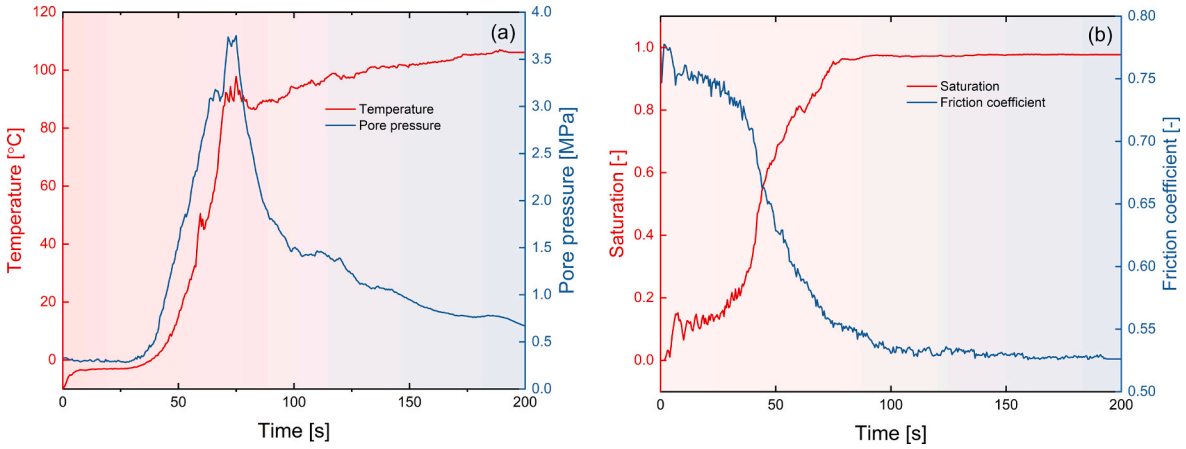

Fig. 20. Evolution profiles of field variables within the shear zone: (a) temperature and pore pressure; (b) saturation and friction coefficient.

incorporated to account for sliding interactions between the multiphase porous continuum and the basal terrain, including frictional heating and thermal pressurization effects. The proposed framework's validity was initially established by modelling the freezing of a semi-infinite porous medium. Its capabilities to model thermal pressurization were further evidenced by simulating frictional heating in two scenarios: an elastic rock-ice block sliding at controlled velocity and an elastoplastic rock-ice mixture sliding on an inclined surface. The framework effectively reproduces Lamplugh's runout (10.5 km) by resolving two key THM dominated hypermobility mechanisms: (i) thermal pressurization resulting from frictional heating and (ii) basal lubrication caused by ice-water phase transitions. This comprehensive modelling approach successfully explains the event's exceptional mobility—a phenomenon that cannot be adequately accounted for by traditional single-phase mechanical models.

To facilitate comparison, we have selected the two-dimensional (2D) Lamplugh rock-ice avalanche as the illustrative case for this paper. Crucially, our framework is inherently versatile and can be seamlessly applied to model rock-ice avalanches across complex three-dimensional (3D) natural terrains (Lei et al., 2022). However, such applications would necessitate high-resolution pre- and post-event 3D DEMs, along with detailed field investigations and seismic signal analysis for calibrating the THM-coupled model. For future work, the proposed modelling framework should be extended to incorporate additional key physical processes that critically influence landslide dynamics, such as the particle breakage of ice blocks within the rock–ice mixture and the mass entrainment along the sliding path. Their integration, informed by existing works (Wei et al., 2024; Jiang et al., 2025), will lead to a more robust and physically consistent simulation of real-world rock-ice avalanches, thereby significantly enhancing the model's predictive capabilities.

CRediT authorship contribution statement

Xiaoqin Lei: Writing – original draft, Visualization, Validation, Software, Methodology, Investigation, Funding acquisition, Conceptualization. **Siming He:** Supervision, Funding acquisition, Formal analysis. **Changbing Qin:** Methodology, Investigation, Formal analysis. **Jidong Zhao:** Writing – review & editing, Supervision, Investigation, Funding acquisition. **Gordon G.D. Zhou:** Investigation, Funding acquisition. **Liu Ming:** Visualization, Data curation.

Declaration of competing interest

The authors declare that they have no known competing financial interests or personal relationships that could have appeared to influence the work reported in this paper.

Acknowledgements

The research is supported by National Natural Science Foundation of China (Nos. 42372330 and 52439001), National Key Research and Development Program of China (No.2022YFF0800604), Sichuan Science and Technology Program (No. 2024NSFSC0102), Science and Technology Research Program of Institute of Mountain Hazards and Environment, Chinese Academy of Sciences (Nos. IMHE-ZYTS-12 and

IMHE-CXTD-01), Research Grants Council of Hong Kong (GRF 16212724).

Data availability

No data was used for the research described in the article.

References

Bardenhagen, S.G., Brackbill, J.U., Sulsky, D., 2000. The material-point method for granular materials. Comput. Methods Appl. Mech. Eng. 187, 529–541. https://doi.org/10.1016/S0045-7825(99)00338-2.

Bardenhagen, S.G., Kober, E.M., 2004. The generalized interpolation material point method. Comput. Model. Eng. Sci. 5, 477–495. https://doi.org/10.3970/cmes.2004.005.477.

Bekele, Y.W., Kyokawa, H., Kvarving, A.M., Kvamsdal, T., Nordal, S., 2017. Isogeometric analysis of THM coupled processes in ground freezing. Comput. Geotech. 88, 129–145. https://doi.org/10.1016/j.compgeo.2017.02.020.

Bessette-Kirton, E.K., 2016. Analysis of landslide volume, structures, and kinematics from satellite imagery of the 2016 Lamplugh rock avalanche, Glacier Bay National Park and Preserve, Alaska. Color. Sch. Mines.

Bessette-Kirton, E.K., Coe, J.A., Zhou, W., 2018. Using stereo satellite imagery to account for ablation, entrainment, and compaction in volume calculations for rock avalanches on glaciers: application to the 2016 Lamplugh rock avalanche in Glacier Bay National Park Alaska. J. Geophys. Res. Earth Surf. 123, 622–641. https://doi.org/10.1002/2017JF004512.

Brackbill, J., 1988. The ringing instability in particle-in-cell calculations of low-speed flow. J. Comput. Phys. 75, 469–492. https://doi.org/10.1016/0021-9991(88)90123-4.

Bui, H.H., Fukagawa, R., Sako, K., Ohno, S., 2008. Lagrangian meshfree particles method (SPH) for large deformation and failure flows of geomaterial using elastic-plastic soil constitutive model. Int. J. Numer. Anal. Meth. Geomech. 32, 1537–1570. https://doi.org/10.1002/nag.688.

Campbell, S., Cleary, P.W., Hopkins, M., 1995. Large-scale landslide simulations: global deformation, and Basal frictio. J. Geophys. Res. Solid Earth 100, 8045–8499. https://doi.org/10.1029/94JB00937.

Coe, J.A., Bessette-Kirton, E.K., Geertsema, M., 2018. Increasing rock-avalanche size and mobility in Glacier Bay National Park and Preserve, Alaska detected from 1984 to 2016 Landsat imagery. Landslides 15, 393–407. https://doi.org/10.1007/s10346-017-0879-7.

Coussy, O., 2004. Poromechanics. John Wiley & Sons Ltd.

De Blasio, F.V., 2014. Friction and dynamics of rock avalanches travelling on glaciers. Geomorphology 213, 88–98. https://doi.org/10.1016/j.geomorph.2014.01.001.

Dong, Z.B., Su, L.J., Hu, B.L., Miao, S.S., 2024. Friction behaviors and flow resistances of rock-ice. Cold Reg. Sci. Technol. 220, 104130. https://doi.org/10.1016/j.coldregions.2024.104130.

Dufresne, A., Wolken, G.J., Hibert, C., Bessette-Kirton, E.K., Coe, J.A., Geertsema, M., Ekström, G., 2019. The 2016 Lamplugh rock avalanche, Alaska: deposit structures and emplacement dynamics. Landslides 16, 2301–2319. https://doi.org/10.1007/s10346-019-01225-4.

Fan, X., Feng, Z., Ni, T., Deng, Y., Zhang, J., Dai, L., 2025. The friction behavior of rock-ice avalanches in relation to rock-ice segregation: insights from flume physical experiments. J. Geophys. Res. Earth Surf. 130. https://doi.org/10.1029/2024JF007904.

Fan, X., Yunus, A.P., Yang, Y., Srikrishnan, S.S., Zou, C., Dai, L., Dou, X., Narayana, A.C., Avtar, R., Xu, Q., Huang, R., 2021. Imminent threat of rock-ice avalanches in High Mountain Asia. SSRN Electron. J. 0–26. https://doi.org/10.2139/ssrn.3989497.

Fish, A.M., Zaretsky, Y.K., 1997. Ice strength as a function of hydrostatic pressure and temperature. US Army CRREL Rep. 97–6, 23.

Gnyawali, K.R., Xing, A., Zhuang, Y., 2020. Dynamic analysis of the multi-staged ice–rock debris avalanche in the Langtang valley triggered by the 2015 Gorkha earthquake Nepal. Eng. Geol. 265, 105440. https://doi.org/10.1016/j.enggeo.2019.105440.

He, C., Liu, E., He, S., Wu, Y., Yin, X., Wang, J., Sun, Y., 2021. A thermo-poro-mechanical model for catastrophic landslides under unsaturated conditions. J. Hydrol. 601, 126810. https://doi.org/10.1016/j.jhydrol.2021.126810.

He, C., Liu, E., He, S., Zhang, J., Wei, H., 2023. On the supraglacial rock avalanches: thermo-hydro-mechanical analysis considering ice-water phase transition. Geomorphology 422, 108550. https://doi.org/10.1016/j.geomorph.2022.108550.

Jiang, R., Zhang, L., Lu, W., Peng, D., He, X., Xiao, S., Wei, M., 2025. A numerical model for cascading glacier mass flow analysis (GMFA): erosion-deposition dynamics, phase changes, and multi-hazard chain transformations. J. Rock Mech. Geotech. Eng. https://doi.org/10.1016/j.jrmge.2025.02.010.

Kääb, A., Jacquemart, M.N., Gilbert, A., Leinss, S., Girod, L., Huggel, C., Falaschi, D., Ugalde, F., Petrakov, D., Chernomorets, S., Dokukin, M., Paul, F., Gascoin, S., Berthier, E., Kargel, S., 2021. Sudden large-volume detachments of low-angle mountain glaciers - more frequent than thought? Cryosphere 15, 1751–1785. https://doi.org/10.5194/tc-15-1751-2021.

Lei, X., Chen, X., Yang, Z., He, S., Zhu, L., Liang, H., 2022. A simple and robust MPM framework for modelling granular flows over complex terrains. Comput. Geotech. 149, 104867. https://doi.org/10.1016/j.compgeo.2022.104867.

Lei, X., He, S., Abed, A., Chen, X., Yang, Z., Wu, Y., 2021a. A generalized interpolation material point method for modelling coupled thermo-hydro-mechanical problems. Comput. Methods Appl. Mech. Eng. 386, 114080. https://doi.org/10.1016/j.cma.2021.114080.

Lei, X., He, S., Chen, X., Yang, Z., Dong, Y., Wang, L., 2024. MPM simulation of frictional heating–induced hypermobility of landslides. Landslides 21, 2273–2287. https://doi.org/10.1007/s10346-024-02269-x.

Lei, X., He, S., Wu, L., 2021b. Stabilized generalized interpolation material point method for coupled hydro-mechanical problems. Comput. Part. Mech. 8, 701–720. https://doi.org/10.1007/s40571-020-00365-y.

Lei, X., Wong, H., Fabbri, A., Limam, A., Cheng, Y.M., 2014. A thermo-chemo-electro-mechanical framework of unsaturated expansive clays. Comput. Geotech. 62, 175–192. https://doi.org/10.1016/j.compgeo.2014.07.004.

Liu, W., He, S., 2024. A simplified single-phase depth-averaged model for rock-ice avalanche movement considering ice melting. Eng. Geol. 337, 107600. https://doi.org/10.1016/j.enggeo.2024.107600.

McKenzie, J.M., Voss, C.I., Siegel, D.I., 2007. Groundwater flow with energy transport and water-ice phase change: numerical simulations, benchmarks, and application to freezing in peat bogs. Adv. Water Resour. 30, 966–983. https://doi.org/10.1016/j.advwatres.2006.08.008.

Nairn, J.A., 2013. Modeling imperfect interfaces in the material point method using multimaterial methods. C. - Comput. Model. Eng. Sci. 92, 271–299.

Nairn, J.A., Bardenhagen, S.G., Smith, G.D., 2018. Generalized contact and improved frictional heating in the material point method. Comput. Part. Mech. 5, 285–296. https://doi.org/10.1007/s40571-017-0168-1.

Pinyol, N.M., Alvarado, M., Alonso, E.E., Zabala, F., 2018. Thermal effects in landslide mobility. Géotechnique 68, 528–545. https://doi.org/10.1680/jgeot.17.P.054.

Pudasaini, S.P., Krautblatter, M., 2014. A two-phase mechanicalmodel for rock-ice avalanches. J. Geophys. Res. F: Earth Surf. 119, 2272–2290. https://doi.org/10.1002/2014JF003183.

Ren, Y., Yang, Q., Cheng, Q., Cai, F., Su, Z., 2021. Solid-liquid interaction caused by minor wetting in gravel-ice mixtures: a key factor for the mobility of rock-ice avalanches. Eng. Geol. 286, 106072. https://doi.org/10.1016/j.enggeo.2021.106072.

Richardson, S.D., Reynolds, J.M., 2000. An overview of glacial hazards in the Himalayas. Quat. Int. 65–66, 31–47. https://doi.org/10.1016/S1040-6182(99)00035-X.

Sansone, S., Zugliani, D., Rosatti, G., 2021. A mathematical framework for modelling rock-ice avalanches. J. Fluid Mech. 919, 1–53. https://doi.org/10.1017/jfm.2021.348.

Schneider, D., Kaitna, R., Dietrich, W.E., Hsu, L., Huggel, C., McArdell, B.W., 2011. Frictional behavior of granular gravel-ice mixtures in vertically rotating drum experiments and implications for rock-ice avalanches. Cold Reg. Sci. Technol. 69, 70–90. https://doi.org/10.1016/j.coldregions.2011.07.001.

Shugar, D.H., Jacquemart, M., Shean, D., Bhushan, S., Upadhyay, K., Sattar, A., Schwanghart, W., McBride, S., de Vries, M.V.W., Mergili, M., Emmer, A., Deschamps-Berger, C., McDonnell, M., Bhambri, R., Allen, S., Berthier, E., Carrivick, J.L., Clague, J.J., Dokukin, M., Dunning, S.A., Frey, H., Gascoin, S., Haritashya, U.K., Huggel, C., Kääb, A., Kargel, J.S., Kavanaugh, J.L., Lacroix, P., Petley, D., Rupper, S., Azam, M.F., Cook, S.J., Dimri, A.P., Eriksson, M., Farinotti, D., Fiddes, J., Gnyawali, K.R., Harrison, S., Jha, M., Koppes, M., Kumar, A., Leinss, S., Majeed, U., Mal, S., Muhuri, A., Noetzli, J., Paul, F., Rashid, I., Sain, K., Steiner, J., Ugalde, F., Watson, C.S., Westoby, M.J., 2021. A massive rock and ice avalanche caused the 2021 disaster at Chamoli Indian Himalaya. Science (80-) 373, 300–306. https://doi.org/10.1126/science.abh4455.

Soga, K., Alonso, E., Yerro, A., Kumar, K., Bandara, S., 2016. Trends in large-deformation analysis of landslide mass movements with particular emphasis on the material point method. Géotechnique 66, 248–273. https://doi.org/10.1680/jgeot.15.LM.005.

Sosio, R., Crosta, G.B., Chen, J.H., Hungr, O., 2012. Modelling rock avalanche propagation onto glaciers. Quat. Sci. Rev. 47, 23–40. https://doi.org/10.1016/j.quascirev.2012.05.010.

Wang, T., Huang, T., Shen, P., Peng, D., Zhang, L., 2023. The mechanisms of high mobility of a glacial debris flow using the Pudasaini-Mergili multi-phase modeling. Eng. Geol. 322, 107186. https://doi.org/10.1016/j.enggeo.2023.107186.

Wei, H., Liu, E., Wei, X., He, C., Chen, L., Li, Q., 2024. Thermo-hydro-mechanical (THM) analysis of rock-ice avalanches: considering the effects of particle breakage in the sliding zone. Cold Reg. Sci. Technol. 219. https://doi.org/10.1016/j.coldregions.2024.104123.

Yang, Q., Su, Z., Cheng, Q., Ren, Y., Cai, F., 2019. High mobility of rock-ice avalanches: Insights from small flume tests of gravel-ice mixtures. Eng. Geol. 260, 105260. https://doi.org/10.1016/j.enggeo.2019.105260.

Yerro, A., Alonso, E.E., Pinyol, N.M., 2015. The material point method for unsaturated soils. Géotechnique 65, 201–217. https://doi.org/10.1680/geot.14.P.163.

Yu, J., Zhao, J., Zhao, S., Liang, W., 2024. Thermo-hydro-mechanical coupled material point method for modeling freezing and thawing of porous media. Int. J. Numer. Anal. Meth. Geomech. 48, 3308–3349. https://doi.org/10.1002/nag.3794.

Zhang, T., Wang, W., Shen, Z., An, B., 2024. Increasing frequency and destructiveness of glacier-related slope failures under global warming. Sci. Bull. 69, 30–33. https://doi.org/10.1016/j.scib.2023.09.042.

Zhao, C., Yang, W., Westoby, M., An, B., Wu, G., Wang, W., Wang, Z., Wang, Y., Dunning, S., 2021. Brief communication: a ~ 50 Mm 3 ice-rock avalanche on 22 March 2021 in the Sedongpu valley, southeastern Tibetan Platea. Cryosph. Discuss. 1–11. https://doi.org/10.5194/tc-2021-306.

Zhao, T., Crosta, G.B., 2018. On the dynamic fragmentation and lubrication of coseismic landslides. J. Geophys. Res. Solid Earth 123, 9914–9932. https://doi.org/10.1029/2018JB016378.